3DVAR and Cloud Analysis with WSR-88D Level-II Data for the Prediction of the Fort Worth Tornadic Thunderstorms Part I: Cloud Analysis and its Impact

Ming Hu[1,2], Ming Xue*[1,2], and Keith Brewster[1]
[1]Center for Analysis and Prediction of Storms
[2]School of Meteorology
University of Oklahoma, Norman, OK 73019, USA

Submitted to Monthly Weather Review
Submitted August 2004
Revised May 30, 2005

*Corresponding Author Address:
Dr. Ming Xue,
School of Meteorology, University of Oklahoma,
100 East Boyd, Norman, OK 73019, USA
E-mail: mxue@ou.edu.

ABSTRACT

In this two-part paper, the impact of Level-II WSR-88D reflectivity and radial velocity data on the prediction of a cluster of tornadic thunderstorms in the Advanced Regional Prediction System (ARPS) model are studied. Radar reflectivity data are used primarily in a cloud analysis procedure that retrieves the amount of hydrometeors and adjusts in-cloud temperature, moisture and cloud fields, while radial velocity data are analyzed through a 3DVAR scheme that contains a mass divergence constraint in the cost function. In Part I, the impact of the cloud analysis and modifications to the scheme is examined while Part II focuses on the impact of radial velocity and the mass divergence constraint.

The case studied is that of the 28 March, 2000 Fort Worth tornado outbreaks. The same case was studied by Xue et al. (2003) using the ARPS Data Analysis System (ADAS) and an earlier version of the cloud analysis procedure with WSR-88D Level-III (NIDS) data. Since then, several modifications to the cloud analysis procedure, including those to the in-cloud temperature adjustment and the analysis of precipitation species, have been made. They are described in detail with examples.

The assimilation and predictions use a 3-km grid nested inside a 9-km one. The Level-II reflectivity data are assimilated, through the cloud analysis, at 10 minute intervals in a one hour period that ends a little over one hour preceding the first tornado outbreak. Experiments with different settings within the cloud analysis procedure are examined. It is found that the experiment using the improved cloud analysis procedure with reflectivity data can capture the important characteristics of the main tornadic thunderstorm more accurately than the experiment using the early version of cloud analysis. The contributions of different modifications to the above improvements are investigated.

1. Introduction

The development of high-resolution nonhydrostatic models and the rapid increase of computer power are making the explicit prediction of thunderstorms a reality (Droegemeier 1990; Lilly 1990; Droegemeier 1997; Xue *et al.* 2003, Xue03 hereafter). Data assimilation plays an important role in providing an accurate initial condition for the model forecast. The operational WSR-88D Doppler radar network of the United States (Crum and Alberty 1993) is a key source of data for initializing storm-scale numerical weather prediction (NWP) models as it is the only operational platform capable of providing observations of spatial and temporal resolutions sufficient for resolving convective storms.

The analysis of radar data to arrive at a complete set of initial conditions for a NWP model is challenging, because radars only observe a very limited set of parameters, the most important being the radial velocity and reflectivity. Their spatial coverage is often incomplete. To determine atmospheric state variables that are not directly observed, certain retrieval or assimilation techniques have to be used.

Four-dimensional variational (4DVAR) data assimilation, which obtains a full set of model initial conditions that provides the best fit between the model solution and radar observations within a time (assimilation) window, is considered ideal for this purpose. Some encouraging 4DVAR results with both simulated and real radar data have been obtained by Sun et al. (1991; 1997; 1998). On the other hand, the complexity of developing and maintaining the adjoint code needed by a 4DVAR system and the high computational cost of 4DVAR technique for high-resolution applications are limiting its use in research and operation. Another relatively new technique is the ensemble Kalman filter (EnKF) method, which has been shown recently to produce single-Doppler radar analyses of thunderstorms that are of similar quality as the 4DVAR

analysis (Snyder and Zhang 2003; Zhang et al. 2004; Tong and Xue 2005). While also expensive because of the need for running an analysis and forecast ensemble of significant sizes, EnKF method is easier to implement and is much more flexible.

Other simpler, yet faster, methods exist that attempt to retrieve unobserved variables from the radar data. The retrieved state variables can then be analyzed into the model initial conditions. The wind retrieval methods include the so-called simple adjoint method (Qiu and Xu 1992; Qiu and Xu 1994; Xu *et al.* 1994; Gao *et al.* 2001) and two-scalar method of Shapiro et al. (1995), among others. The latter has been used by Weygandt et al. (2002a) to initialize a numerical model. Additionally, the retrieved three-dimensional wind fields at more than one time level can be used to retrieve thermodynamic fields (Gal-Chen 1978). The retrieved fields can then be combined via an analysis procedure, as is done in Weygandt et al. (2002b). Such multi-step procedures have an advantage in being able to make use of multiple radar volume scans in an inexpensive way, but the involvement of multiple steps and the use of retrieved instead of direct observations make the optimality of analysis difficult to achieve.

Another alternative is to analyze the radial velocity data directly via a three-dimensional variational (3DVAR) analysis procedure. Certain dynamic or equation constraints can be built into the 3DVAR cost function with relative ease. Such a system has been developed within the ARPS model (Xue *et al.* 1995; 2000; 2001) framework and documented in Gao et al. (2002; 2004). It is used in this study to analyze radial velocity and other conventional observations. The 3DVAR method is theoretically less optimal than 4DVAR because it lacks a time dimension, but is much faster. In our study, we bring in the time dimension therefore utilize data over a period of time by performing intermittent assimilation cycles.

The use of reflectivity data for the purpose of thermodynamic and microphysical

retrievals and analysis is not straightforward. Semi-empirical rules can be used to aid the analysis of these fields. In the current ARPS system, this is done with a complex cloud analysis procedure. This cloud analysis procedure has evolved from that used in the Local Analysis and Prediction System (LAPS, Albers *et al.* 1996) with previous modifications documented by Zhang et al (1998) and Zhang (1999). It is a component of both the ARPS 3DVAR and ADAS (ARPS Data Analysis System, Brewster 1996) analysis systems.

In Xue03, the Bratseth (1986) scheme-based ADAS with the then-current version of cloud analysis is applied to the 28 March, 2000 Fort Worth tornado case. In that work, Level-III (NIDS) reflectivity data are assimilated at 15-minute intervals. While their results are encouraging, significant discrepancies in the predicted storms are noted in the paper. In this work, as an attempt to improve the assimilation and forecast, we replace the ADAS with the ARPS 3DVAR and in addition assimilate the radial velocity data directly, with a mass divergence constraint to couple the wind components together. We employ an updated version of the cloud analysis that includes a different scheme for temperature adjustment in the cloud regions and modifications to other parts of the procedure. In addition, we use the full-volume Level II instead of the Level III data that are of reduced precision and only include the 4 lowest tilts of data.

In Part I of this study (this paper), we discuss several modifications to the cloud analysis procedure and their impact. In Part II (Hu et al. 2005), we will focus on the discussion of using radial velocity data via the 3DVAR procedure. The organization of this paper is as follows. In Section 2, the basic ARPS 3DVAR scheme is introduced, while the cloud analysis scheme and the modifications to it are described in detail. In Section 3, we introduce the case studied and the design of a set of experiments for investigating the impact of the updated cloud analysis and individual modifications. A detailed comparison among experiments is presented in Section 4.

Results are then summarized in Section 5.

2. The analysis schemes

a. The basic ARPS 3DVAR scheme

In this part, the conventional data are analyzed with the ARPS 3DVAR. The main features of the ARPS 3DVAR are introduced here while more details can be found in Gao et al (Gao et al. 2004) and in Part II.

The ARPS 3DVAR uses an incremental form of cost function that includes the background, observation and equation constraint terms. The analysis variables include the three wind components (u, v, and w), potential temperature (θ), pressure (p) and water vapor mixing ratio (q_v). Hydrometeors are not analyzed variationally. In the current system, the cross-correlations between variables are not included in the background error covariance. The spatial covariances of background error are modeled by a recursive filter. The observation errors are assumed to be uncorrelated, hence observation error covariance is a diagonal matrix. The observation error variances are specified according to the estimated errors. Multiple analysis passes are used to analyze different data types with different filter scales in order to account for the variations in the observation spacing among different data sources. The choice of the filter scales is guided by the density of observational network to which filter is applied.

b. The cloud analysis

The cloud analysis procedure incorporates cloud reports from surface observations from Global Observing System (GOS) of the World Meteorological Organization (WMO), standard Aviation Routine Weather Reports (METARs), geostationary satellite infrared and visible imagery data, and radar reflectivity data to construct three-dimensional cloud and precipitate

fields. The products of the analysis package include three-dimensional cloud cover, cloud liquid and ice mixing ratios, cloud and precipitate types, icing severity index, and rain, snow and hail mixing ratios. Cloud base, top and cloud ceiling fields are also derived. A latent heat adjustment to temperature based on added adiabatic liquid water content is applied in order to make the in-cloud temperature consistent with the cloud fields. More details on the package can be found in the references cited in Section 1.

The above version of the cloud analysis was used in Xue03. Since then, several improvements have been made to the cloud analysis procedure in order to make it more suitable for thunderstorm initialization. Some improvements are described in Brewster (2002). In this section, we introduce the original and updated cloud analysis schemes and the corresponding modifications, together with example analyses.

1). The analysis of precipitation species

a) The reflectivity equations

Reflectivity equations that link the precipitation species or hydrometeors (rain, snow and hail mixing ratios in our case) with the reflectivity are needed to determine the former from the latter. The process of determination also utilizes information, such as temperature, from the background analysis, which usually is an analysis that has already incorporated other observations.

In our updated cloud analysis, the three equations that define the contributions of rain, snow and hail to the total reflectivity is based on Smith, Myers and Orville (SMO1975) and the exact form used can be found in Tong and Xue (2005). Based on precipitation types identified according to reflectivity and the background state, the rain, snow and hail mixing ratios are determined using the reflectivity equations. We refer to this precipitation species determination

procedure the SMO scheme. In the cloud analysis procedure used by Xue03, the rainwater mixing ratio is retrieved using the Kessler reflectivity equation (Kessler 1969), and snow and hail are retrieved using Rogers and Yau (1989) reflectivity formula. This procedure is referred to as the KRY scheme.

The SMO reflectivity equations were derived based on cloud physics and hydrometeor backscattering models while the KRY equations were based on curve and parameter fitting to observations. The SMO scheme is believed to be more accurate.

b) The initial determination of hydrometeors from reflectivity

To perform the cloud analysis, the reflectivity data are first remapped to the analysis grid using a procedure that employs a local least squares fitting to the polar-coordinate data assuming that the reflectivity varies quadratically in the x- and y-directions and linearly in the vertical. Quality control, including screening for anomalous propagation, is applied in the remapping step.

In the SMO scheme, within the radar scan volume, the grid points are classified into clear or precipitation-filled categories based on a 10 dBZ reflectivity threshold. This threshold is chosen because most non-hydrometeor targets, such as ground clusters, have reflectivity values less than 10 dBZ but often above 0 dBZ. Where observations are flagged as missing, the corresponding grid points are categorized as missing too. The precipitation species at the precipitation-filled points are retrieved from the observed reflectivity while those at the clear points are set to zero. For the points below the lowest radar elevation, the SMO scheme uses the background values but limits the total mixing ratio of the hydrometeors to be no larger than the maximum of total mixing ratios in the column above.

In the KRY scheme, the threshold is set at 0 dBZ instead. The points with reflectivity greater than 0 dBZ are considered to be precipitation-filled and all other points are flagged as

missing. For the points below the lowest radar elevation, the KRY scheme sets the precipitation species to zero. In both cases, for the missing points and in the areas beyond the radar range, the background values are used in the final analysis.

Figure 1 shows, as an example, the initial determinations of precipitation species (referred to as observation-based retrievals hereafter) by the KRY (left column) and SMO (right column) schemes. The background field in this case is a 10-minute ARPS model forecast at 3 km resolution and the radar data are from the Fort Worth, Texas WSR-88D radar and are valid at 2250 UTC, 28 March, 2000. It can be seen that the KRY scheme gives much more hail and rain but less snow than the SMO scheme, reflecting the warm rain root of the KRY scheme. In the rain field of SMO scheme, the large values under the lowest radar elevation came from the forecast background.

c) The final analysis of hydrometeors

The next step of hydrometeor analysis consists of a judiciary combination of the background values with those determined from reflectivity observations. In the scheme used in Xue03 (denoted as Xue03 scheme), the greater one among the background and observation-based values is taken. In our updated scheme, based on the belief that the radar-observed precipitation is much more reliable than the model prediction, the values determined from the observations are used whenever the latter are available. This new procedure helps remove spurious precipitation in the forecast background. With the updated scheme, where valid radar observation is present, the reflectivity-based retrieval is chosen over the background value.

As an example, we show in Fig. 2 the final analysis of precipitation species by the Xue03 scheme, which corresponds to the initial determination shown in the left column of Fig. 1. It can be seen that in this case the background values dominate the final analysis for all three species.

The reflectivity fields calculated from the background hydrometeors, the final analysis of Xue03 scheme and that of updated scheme are plotted in Fig. 3. We can see that the reflectivity from the Xue03 scheme largely mirrors the background, while the reflectivity using the updated scheme shows more detailed observed structures inside the storms.

2). The analysis of cloud water and cloud ice

To estimate cloud water and cloud ice mixing ratios, the adiabatic liquid water content (ALWC) is estimated by assuming a moist-adiabatic ascent from cloud base to cloud top. A reduction is applied to the ALWC to account for entrainment. In the scheme used by Xue03, the curve of reduction was determined from field data collected largely from isolated towering cumulus clouds (Warner 1970). This curve tends to produce liquid and ice water contents that are too low. In the cases of supercell and widespread thunderstorms, clouds have much larger vertical and horizontal extent and less entrainment in the center of storm cells. Based on this consideration, a new entrainment curve is devised in the updated scheme to limit the reduction of cloud water and ice due to entrainment. Fig. 4 shows the analyses of cloud water and cloud ice using the curve of Xue03 (left) and the new curve (right). The increase in cloud mixing ratio with the latter is evident. In our experiments at 3 km horizontal resolution, the cloud water and cloud ice analyzed using the updated scheme can usually sustain the model reflectivity for no less than 10 minutes.

3). In-cloud thermal adjustment

Temperature adjustment associated with precipitating clouds is very important in sustaining existing convection. In the cloud analysis used in X03, the temperature adjustment is calculated from the latent heat release corresponding to the added cloud water and ice (referred

to as the latent heat scheme). In the updated scheme, a moist-adiabatic temperature profile with the same entrainment factor as applied to the cloud water is used to adjust the temperature after determination of cloud and precipitation contents. This adjustment scheme is more consistent with the physics of a convective storm because it reflects the temperature change in an ascending moist air parcel. The typical temperature adjustments due to the two schemes are plotted in Fig. 5. The profile of horizontally averaged temperature increments show that the moist-adiabat-based scheme heats the atmosphere through a greater depth, while the latent heat scheme warms the atmosphere more at the middle and lower levels where cloud water and ice are concentrated (Fig. 5a). The difference in the temperature adjustments of the two schemes at 4.5 km MSL shown in Fig. 5b has a similar pattern as the observed reflectivity.

3. ARPS data assimilation and forecast systems and design of experiments

As stated earlier, in this study, we apply our 3DVAR and the updated cloud analysis schemes to the Fort Worth tornado case studied by Xue03. We evaluate the performance of the analysis mainly by examining the quality of the subsequent forecast.

On 28 March, 2000, two tornadoes were observed in the Fort Worth, Texas (TX) area. One reached F2 intensity (maximum winds 51 m s^{-1} to 70 m s^{-1}) and struck downtown Fort Worth at around 6:15 pm LST 28 March (0015 UTC 29 March), 2000. The tornado funnel developed directly over the city, descended, and stayed on the ground for at least 15 minutes. The tornado caused extensive damage to several structures, including high-rise buildings. It directly caused two fatalities and many injuries. The parent storm also brought torrential rains and softball-size hail stones, causing two deaths from flooding in the eastern portion of Tarrant County (highlighted in Fig. 6a), near Arlington, and one additional death due to hail. Another tornado from the same complex of storms touched down in south Arlington, approximately 25

kilometers east of Fort Worth, about 30 minutes after the Fort Worth tornado, at about 7:00 pm LST 28 March (0100 UTC 29 March), 2000. These tornadoes have special significance because they struck the center of a major metropolitan area.

The mesoscale and synoptic scale settings in which the tornadic thunderstorms occurred are described in Xue03. The primary goal of this work is to test the impact of Level II WSR-88D reflectivity and radial velocity data on the ability of a high-resolution model and its data assimilation system to initialize and forecast pre-existing thunderstorms. The capabilities of the ARPS 3DVAR and the improved cloud analysis procedure are also examined through real data experiments. In Part I of this paper, we will focus on the cloud analysis procedure and its impact; the impact of assimilating radial velocity data are discussed in Part II. Because all thunderstorms to be studied occurred within the range of Fort-Worth (KFWS) radar during the period of assimilation, only data from KFWS are used.

Similar to the experiments reported by Xue03, two one-way nested grids are used here, with the resolutions of 9 and 3 km, respectively. The two grids cover areas of 1000 ×1000 and 450×300 km^2, respectively, and the vertical grid spacing is increased from 20 m at the surface to about 770 m at the model top located at 21.1 km height**.** The same model grids are used for the analysis and forecast, and the increased near-surface vertical resolution allows for better resolution of the boundary layer features. These model settings are essentially the same as in Xue03, except that an updated version of ARPS is used. Specifically, we employ full model physics, including a two-layer soil-vegetation model and Lin et al (1983) ice microphysics without cumulus parameterization. At 3 km resolution, cumulus parameterization is usually not needed while the 9 km resolution falls into a 'gray' area where neither explicit nor parameterization precipitation physics works well. A corresponding 9-km experiment with the

Kain-Fritsch cumulus parameterization scheme led to poorer results on the 3 km grid.

The 9-km grid is initialized at 1800 UTC 28 March, from a single 3DVAR analysis that combined rawinsonde, wind profiler, METAR surface observations and Oklahoma Mesonet data, using the National Center for Environmental Prediction (NCEP) Eta model 1800 UTC analysis as the background. At the lateral boundaries, the 9-km grid is forced by the Eta 1800 UTC forecasts at 3-hour intervals. No data assimilation is performed for the 9-km grid and the forecast is run for 12 hours, ending at 0006 UTC 29 March. With the primary goal of initializing pre-existing storms, the 3-km grid is started at a later time (2200 UTC), when some of the thunderstorms have already formed and were captured by the KFWS radar.

Different from the 3-km experiments of Xue03, we use the ARPS 3DVAR instead of the ADAS as the analysis tool. Further, we use and examine an improved version of the cloud analysis. In addition, we use Level II instead of Level III data with 10-minute instead of 15-minute intermittent assimilation cycles. As in Xue03, the hour-long assimilation period starts at 2200 UTC and end at 2300 UTC, about 1 hour 15 minutes before the tornado touched down in Fort Worth. The Level II data contain 9 (in the first half an hour) or 14 (in the second half an hour) instead of 4 elevation levels, without Level III's degradation in the radial velocity data precision (Level-III radial velocity data were used in Xue03 through a simple radial velocity adjustment procedure of the ADAS). The reflectivity data are used in the cloud analysis procedure to retrieve cloud and hydrometers fields and to make adjustments to in-cloud temperature and moisture. The radial velocity data are analyzed by the 3DVAR subject to a mass divergence constraint (as detailed in Part II).

Since data representing very different spatial scales are used, we employ the multi-pass strategy available with our 3DVAR system. Specifically, two analysis passes are performed on

the 3-km grid, with each pass using different data types. Filter scales of 120 and 75 km are used in the first and second passes when the wind profiler data and surface data are used, respectively.

The 3-km forecasts start at 2300 UTC 28 March from the assimilated initial conditions and end at 0200 UTC 29 March. Because few surface and upper-air data are available within the 3-km domain during the assimilation period, the storm environment is defined primarily by information carried over from 1800 UTC (when there are more observations) by the 9-km ARPS forecast or from even earlier by the Eta model. The 9-km pre-forecast period is generally helpful in reducing the spin-up time on the 3-km grid for both the assimilation and model forecast.

To investigate the impact of the new cloud analysis, only reflectivity data are employed in the assimilation cycles of the control experiment of this paper (Part I), CNTLZ, at the 3-km resolution. The 3DVAR analysis is used to analyze model state variables but no radial velocity data are used.

The control experiment of Xue03 is repeated in this part for comparison (listed as experiment X03 in Table 1). It uses exactly the same data and configurations except for a slightly different version of the ARPS and ADAS, which are configured as close to those in Xue03 as possible. Differences between our current experiments with X03 were described earlier.

Based on our current control experiment, CNTLZ, three experiments, CTLH, CKRY and CMAX are performed to examine, respectively, the impact of different schemes of in-cloud temperature adjustment, the initial determination of hydrometers from reflectivity and the final analysis of hydrometeors in the X03 and updated cloud analysis procedures (Table 1). Experiment without radar data, NoVRZ, is also conducted for comparison purpose.

4. Results of forecast experiments

In this study, we use reflectivity data, at the original radar elevation levels, as the primary

observations for forecast verification, because there is no other observation with similar temporal and spatial resolutions as the model forecast. The next possible source of information would be the hourly surface observations; since there are less than 20 surface observations within the model domain and they do not provide information on the 3D storm structure, their use for quantitative verification is limited. Rain gauge data do not have sufficient resolution for precipitation verification either.

In this section, the forecast results from experiments CNTLZ, X03, and NoVRZ are first analyzed to investigate the impact of the updated cloud analysis procedure and Level-II WSR-88D reflectivity data. It also serves to establish the improvement of the new configuration over the old one (as used in Xue03). The impacts of each modification in the cloud analysis procedure are then examined by comparing assimilation and forecast results of all experiments except for NoVRZ.

a. Radar observations

Observed reflectivity at 1.45° elevation from Level-II data of the Fort Worth radar (KFWS) at 15-minute intervals for 1 hour starting from 0000 UTC 29 March are plotted in Fig. 6. This hour covers the forecast period in which two tornadoes struck in Tarrant County (one at 0015 UTC at Forth Worth and one at 0100 UTC near Arlington). Tarrant County is highlighted by the bold rectangle in the figure. Downtown Fort Worth and Arlington are marked by black dots in Fig. 6a. Names of most counties to be referenced are also found in Fig. 6a.

Five individual thunderstorms can be identified around Forth Worth from the observed radar reflectivity at 0000 UTC 29 March (Fig. 6a). Storm A is the storm that spawned the downtown Forth Worth and Arlington tornadoes 15 minutes and 1 hour later, respectively. Storm B followed Storm A from the west. It approached Storm A from 0000 UTC to 0045 UTC (Fig. 6a-d) and then merged with Storm A to form a combined storm that is indicated as F (Fig. 6e).

Storms C and C' formed after the end of the assimilation cycles, propagated toward Storm A from the south and also merged into Storm A (Fig. 6) at about 0100 UTC. Storm D is located initially near the northeast corner of Hill County and later propagated northeastward into Ellis County. Storm D formed during the assimilation cycles and remained strong throughout the hour (Fig. 6). It is a significant challenge for the data assimilation and model forecasting system to accurately forecast these individual storms and their complex interactions.

b. Results of experiments CNTLZ and X03

1). Subjective evaluation

Reflectivity fields at the 1.45° elevation (corresponding to the elevation angle of the radar observed reflectivity in Fig. 6) derived from predicted hydrometeors of CNTLZ and X03 are plotted in Fig. 7. The plots show the reflectivity fields from 0000 UTC 29 March, which is 2 hours after the data assimilation cycle is started and 1 hour after the forecast initial time, through 0100 UTC 29 March at 15-minute intervals. The left column of Fig. 7 shows results of X03 while the right column shows the counterparts from CNTLZ.

At 0000 UTC 29 March, the one-hour forecast of CNTLZ exhibits reasonable structures of the storms around Fort Worth (Fig. 6a, Fig. 7b) but with some position errors. Predicted Storm A lags the observation by approximately 20 km. Predicted Storm B only shows as a weak echo and lags the observation by about 20-25 km. The model produces Storm C with a northward displacement of about 5 km and does not produce Storm C'. Considering that little information on Storms C and C' was provided by the assimilation cycles directly, it is encouraging that the model produces Storm C by itself at this time. The model produces an accurate forecast of Storm D, but at the same time, it generates a spurious storm, D', which split from Storm D in the first hour of the forecast and moves north into the southeast corner of Tarrant County. Another

spurious storm appears southwest of Storm A and is labeled as A'. Comparing these storms to their counterparts in X03 (Fig. 7a), they are stronger except for spurious Storm D'. At this time, X03 gives much better position forecast for both Storms A and B than CNTLZ. However, the forecast of X03 misses Storms C and C', and produces a spurious storm, A', southwest of Storm A.

Fifteen minutes later, at 0015 UTC, is the time of the first tornado touchdown, in downtown Fort Worth. Experiment CNTLZ correctly predicts tornadic Storm A strengthening and approaching Forth Worth from the west, although the forecast reflectivity maximum of Storm A still lags the observations (Fig. 6b and Fig. 7d). Predicted Storm B remains weak and lags the observation by about 25 km. Predicted Storm C is located midway between observed Storms C and C'. Storm D is well reproduced by CNTLZ and the spurious Storm D' that appeared earlier has dissipated by this time. The spurious Storm A' has grown and remains southwest of Storm A. In comparison, the storms in X03 moved eastward too quickly in the period from 0000 to 0015 UTC and the reflectivity maximum of Storm A had already passed downtown Fort Worth (Fig. 7c) by 0015 UTC. A weak echo at the center of the western boundary of Johnson County gives the only hint of observed Storm C in X03 forecast. Just to the west of predicted Storm C, spurious Storm A' has developed into a long band-shaped echo connected with Storm A and subsequently sweeps through the weak Storm C. Unlike CNTLZ, spurious Storm D' in X03 remains as a strong northbound storm.

At 0030 UTC, in the CNTLZ forecast, Storm A is nearly colocated with the observed cell except that it extends too broadly in the north-south direction and has two maxima reflectivity centers (Fig. 6c and Fig. 7f). Its shape does suggest an inflow notch on its southeastern flank. At this time, Storm B is not identifiable as a separate storm, though the southwestern quadrant of

Storm A and the northeastern corner of Storm A' overlay the position of Storm B. Predicted Storm C appears as a weak echo that covers location of observed Storm C and C'. There is reason to believe the CNTLZ forecast is a bit fast with the merger of cells that occurs in Tarrant County. Storm D is well reproduced except that it moves a little faster than the observation, and spurious Storm A' still exists with a strong reflectivity center. In the X03 forecast, intense reflectivity composed by Storm A and A' is found extending from Storm A in the northeast corner of Tarrant County through the southwest corner of the county and reaching the center of Hood County (Fig. 7e). This may be due to incorrect positioning of storm A with a 30 km displacement, possibly to be ascribed to a merger with the spurious storm D'.

At 0045 UTC, the main characteristics of Storm A are successfully reproduced in the CNTLZ forecast (Fig. 6d, Fig. 7h). The predicted southern reflectivity maximum of Storm A has intensified and is just south of Arlington. Together with the northern reflectivity maximum of Storm A and the westward-extending part of Storm A, the area of predicted Storm A covers the bulk of the combined area of observed Storms A, B and C. At this time, isolated spurious Storm A' is weak. Predicted Storm D is still few kilometers southeast of the observed cell. In the X03 forecast, the Storm D' has merged with Storm A and has made the latter move into the center of Dallas County (Fig. 7g). The northeast part of Storm A' is in the same area as the south center of Storm A in CNTLZ and is also near south Arlington.

By 0100 UTC, observed Storms A, B and C had merged into one storm F and produced the Arlington tornado (Fig. 6e). In CNTLZ run (Fig. 7j), the location of Storm A corresponds to the correct location of observed storm F, while in the X03 forecast (Fig. 7i), Storm A leads the observed Storm F by approximately 35 km and Storm A' covers part of Storm F, but its center deviates from the main part of observed F by 15 km. At this time the position forecast for Storm

D in CNTLZ is also more accurate than that of X03.

The surface wind and temperature fields from CNTLZ and X03 are plotted in Fig. 8. At the time of the downtown Fort Worth tornado, approximately 0015 UTC, CNTLZ predicts areas of strong convergence along the gust front produced by tornadic Storm A approaching downtown Fort Worth from the northwest (Fig. 8b), while in experiment X03, the convergence coincident with the gust front of Storm A is much weaker and has passed downtown Fort Worth (Fig. 8a). At 0045 UTC, the gust front and low-level convergence related to Storm A are still strong and approach south Arlington in the CNTLZ run (Fig. 8d). In X03 (Fig. 8c), the gust front of Storm A is weaker and Storm A has moved east of Tarrant County. Almost the entire county is covered by the cold pool of Storm A' at this time.

From the above comparison, it is found that using the new cloud analysis procedure with the Level-II reflectivity data through the 10-minute assimilation cycles improves the prediction of the tornadic thunderstorms, over the results of Xue03 (or equivalently experiment X03 here). In the CNTLZ run, the tornadic thunderstorm A, appearing with high reflectivity and strong low-level convergence centers, approaches and passes downtown Fort Worth and Arlington around the times of tornado occurrence, while in X03, the reflectivity center of Storm A and the related gust front move too fast and have obvious location errors during the tornado outbreaks.

2). Evaluation with ETS

Quantitative evaluation of numerical forecast of discrete features such as convective cells is difficult and remains an active area of research. Traditional skill scores, such as the equitable threat score (ETS), which are originally designed for large scale precipitation prediction, have limited utility when applied to small-scale convective system (Baldwin et al. 2002). Due to the predictability limit of individual convective cells and discrete nature of such systems, the

displacement in space of predicted cells are often as large as cells themselves and can make skill scores very low, even when the strength and morphology are well captured by the forecast. Still, to more quantitatively evaluate the quality of forecast, the ETS (Schaefer 1990) of predicted reflectivity fields are calculated against observations.

Figure 9 shows the ETS of predicted reflectivity fields at the 1.45º elevation for the 5, 15, 30 and 45 dBZ thresholds. We can see that the scores decrease quickly in the first hour of forecast then increase in the second hour for all thresholds. This behavior reflects the adjustments of the initial storms in the first hour of forecast. It can be seen that all scores are better for CNTLZ than for X03 from 0030 UTC to 0100 UTC, in agreement with the previous subjective assessment of the forecast cells. Our subjective analysis does suggest that the forecast of CNTLZ is superior at 0015 UTC for Storm A, however, the scores for the entire domain do not reflect this. The reason is that both CNTLZ and X03 have some phase errors in the predictions of Storms A, B, and C, and both contain some spurious storms at this time. The disagreement between the ETS at 0015 UTC and our subjective analysis suggest that the ETS for the entire domain should be used carefully when the phase errors have a significant impact on the scores.

c. Experiments without radar data

In this subsection, we present results from experiment NoVRZ that does not use any radar data. The predicted reflectivity field from experiment NoVRZ mapped to the same elevation as the previous figures is plotted in Fig. 10 at 0030 UTC 29 March, which is in-between the times of the two tornadoes.

Compared to the observed reflectivity (Fig. 6c), experiment NoVRZ completely fails to predict storm cells around Fort Worth (Fig. 10), indicating a failure to build and support storm

cells in a short-term forecast. There are two storm cells to the southwest of Tarrant County and they originated from the 9-km forecast that was used as the background for the initial 3-km analysis at 2200 UTC.

Based on the above results, we conclude that the assimilation of reflectivity data from a single Doppler radar via an efficient intermittent assimilation procedure is effective in building up pre-existing storms in a nonhydrostatic model given a 3-km horizontal resolution. The forecast starting from the assimilated initial condition is able to capture most of the supercell characteristics of the observed storms for a two-hour period.

d. Sensitivity to details of cloud analysis

To identify the impact of each modification in the cloud scheme on the results of assimilation and forecast, three experiments are performed (see Table 1): 1) CTLH, in which in-cloud temperature adjustment is based on latent heat conversion instead of moist adiabatic temperature profile; 2) CKRY, which uses the KRY scheme instead of the SMO scheme to determine the initial values of hydrometeors from reflectivity; and 3) CMAX in which the quantities of the precipitation species are determined by the maximum of background and observation-based retrievals. All other options in these experiments are the same as CNTLZ.

1) Assimilation results

The reflectivity fields at the end of 1 hour assimilation period, mapped to the 1.45° elevation of the KFWS radar are plotted in Fig. 11 for the five experiments together with the corresponding observed field (Fig. 11a) . With CNTLZ (Fig. 11b), the storm structures look similar to the observations, though the interpolation scheme and cloud processing make the features smoother than those observed (Fig. 11a). Given that CNTLZ uses the observation-based

retrievals directly in the analysis, it is expected that the reflectivity after the assimilation matches the observed reflectivity. In contrast, the initial reflectivity in X03 does not capture many details of storm cells (Fig. 11c). In CTLH, the analyzed reflectivity is similar to that of CNTLZ in the area near the radar (Fig. 11d), but has higher reflectivity maxima than their counterparts in CNTLZ in the areas away from the radar because the two experiments have different mid-level temperature fields (c.f., section 2b3). CKRY (Fig. 11e) uses simple radar reflectivity equations to retrieve precipitation species, which result in reflectivity fields smoother than those of CNTLZ. In Fig. 11f, which shows the analyzed reflectivity of CMAX, the influence of the background values of the precipitation species is evident. In this case the maximum value of background and observation-based retrievals is taken as the analysis; at this time the background reflectivity is generally greater than the observations.

The surface wind and temperature fields from these five experiments and from the background before the analysis are plotted in Fig. 12. In this figure the storm-related gust fronts and cold pools are found in all cases. As also noted with the reflectivity fields, CNTLZ (Fig. 12b) presents more storm details than X03 (Fig. 12c). In the surface wind and temperature analyses of CTLH, CKRY, and CMAX (Fig. 12d, e, f), only CTLH shows large differences from CNTLZ; its appearance is more similar to X03. Both CTLH and X03 underestimate the strength of the cold pool and gust front related to Storm A (Fig. 12c, d). This indicates that the formation of cold pool and gust front is sensitive to the choice of temperature adjustment scheme, presumably through the direct effect of the latter on storm intensity.

The strength of the updraft is an important indicator of the vigor of a thunderstorm. Fig. 13 shows the cross section of vertical velocity, w, along a line through Storms A and B (c.f., Fig. 11a). In X03, the updraft related to Storm B is weak and there is no sign of the existence of Storm

A (Fig. 13a), while in CNTLZ (Fig. 13b), two large updraft centers associated with Storms A and B are found. It shows that storms have been built up well through assimilating Level-II reflectivity data by the new cloud analysis procedure. The vertical velocity fields from CMAX, CKRY and CTLH reflect different impacts of each modification (Fig. 13c, d, e). Each of them has one strong updraft center and one weak updraft center. Comparing Fig. 13 to the corresponding surface wind and temperature fields in Fig. 12, it is found that the vertical motion of Storm A is strongly correlated to the strength of the surface cold pool and gust front.

2) Forecast results

In the above subsection, we have seen that assimilation results are obviously affected by the modifications to the cloud analysis procedure. In this subsection, forecasts starting from the results of assimilation are compared in order to make further inferences on the effects of these modifications. Fig. 14 shows the predicted reflectivity mapped to the 1.45° elevation of KFWS radar from CMAX, CKRY, and CTLH near the time of the tornadoes. The surface wind and temperature fields from the same experiments and times are plotted in Fig. 15.

The main characteristics of the predicted storm cluster in CMAX, CKRY and CTLH are similar to that of CNTLZ at the time of the downtown Fort Worth tornado (Fig. 14a, c, e, and Fig. 7d). Focusing on the details of Storm A, it is found that Storm A in CKRY and CTLH has the same shape and position as in CNTLZ, while the storm moves faster in CMAX than in CNTLZ. A similar behavior is shown in the gust fronts related to Storm A: the gust fronts of Storm A in CKRY, CTLH and CNTLZ are in similar positions (Fig. 8b, Fig. 15c, e), while that in CMAX moves faster (Fig. 15a). All three experiments have spurious Storms A' and D' appearing in the forecast at this time (Fig. 14a, c, e).

By 0045 UTC, the differences among CMAX, CKRY, CTLH and CNTLZ have

increased (Fig. 14b, d, f, and Fig. 7h). Storm A in CMAX has obviously led its counterpart in CNTLZ and connected with spurious Storm D'. It then propagates into the center of Dallas County in the next 15 minutes of the forecast, as Storm A does in X03 (Fig. 7i). The northern part of the gust front associated with Storm A in CMAX has reached the east boundary of Tarrant County and the southern part is approaching the southeast corner of the county (Fig. 15b). Although Storm A in CKRY and CTLH has the same position at 0015 UTC, it propagates in different directions in these two experiments during the following half an hour. In CKRY, Storm A moves southeast to the center of Tarrant County and lags Storm A in CNTLZ. In CTLH, Storm A propagates northeast and exits Tarrant County from its northeast corner. In the surface wind and temperature fields of CKRY and CTLH (Fig. 15d, f), the cold pool and gust front of Storm A follow the same motion direction and reach the same position as the reflectivity.

Another big difference among these experiments at 0045 UTC is the behavior of spurious Storm D'. It remains as a strong isolated echo center in CKRY (Fig. 14d), connects with Storm A in CMAX (Fig. 14b), and merges into Storm A in CTLH (Fig. 14f) which partly accounts for the fast motion of Storm A in that experiment. The spurious Storm D' does not exist after 0015 UTC in the forecast of CNTLZ (Fig. 7), while it merges with Storm A at 0030 UTC in the forecast of experiment X03 and causes large location errors of Storm A at 0045 UTC.

The above comparisons show that adjusting in-cloud temperature based on a moist-adiabatic profile and choosing the values of observation-based retrievals over those of background in the updated cloud analysis procedure act to slow down the motion of predicted tornadic Storm A during the period of the tornado occurrence. These two modifications, together with the use of SMO scheme for the initial determination of precipitation species, contribute to

the elimination of spurious Storm D' and avoid the erroneous acceleration of Storm A found in the X03 forecast. For the current case, experiment CNTLZ gives the best forecast for the tornadic thunderstorms during the critical tornado outbreak period.

5. Summary

In this first of our two-part paper, the investigation focuses on the updated cloud analysis procedure used with the Level II WSR-88D reflectivity data. The 28 March, 2000 Fort Worth tornado outbreak observed by the Fort Worth (KFWS) radar is used as a test case which was also studied by Xue et al. (2003). A 3-km grid nested inside a 9-km one is used for both assimilation and prediction experiments. For all 3-km experiments except for X03, a one-hour long assimilation with analysis cycles at 10-minute intervals is performed, which is followed by a three-hour forecast starting from the assimilated initial condition. A total of six 3-km experiments are conducted to investigate the impact of the cloud analysis procedure and its modifications. Among the experiments, X03 is a repeat of the 3 km experiment reported in Xue et al. (2003) and used 15-minute instead of 10-minute analysis cycles.

Starting from an initial condition that assimilates Level-II reflectivity data through the updated cloud analysis procedure, the control experiment CNTLZ successfully reproduces the evolution of the most significant thunderstorms in the Fort Worth tornado case. The forecast captures a storm with strong reflectivity gradients in the hook echo region and a low-level center of strong convergence and rotation that approaches and passes through downtown Fort Worth and Arlington around the time of the tornado occurrences. Compared to a reconstructed experiment following Xue03 that uses an earlier version of the cloud analysis with Level-III reflectivity data, the experiment with all recent modifications to the cloud analysis, CNTLZ, shows reductions in both timing and location errors for the tornadic thunderstorm in the

complex.

Comparing the forecast results of experiments CNTLZ and NoVRZ, it is found that the assimilation of reflectivity data via an efficient intermittent assimilation procedure is critical for capturing the key characteristics of the observed storms in the 3-km forecast.

The analysis shows that the initial state and the evolution of the storm in the forecast can be impacted by each individual modification in the cloud analysis scheme. Adjusting in-cloud temperature based on a moist adiabatic profile and choosing observation-based retrievals of the precipitation species over background values in the cloud analysis can slow the movement of storms and improve the forecast of the tornadic storm. These two modifications, together with the SMO scheme for the initial determination of hydrometeors, prevent a spurious storm from appearing in the forecast.

Adding hydrometeors and adjusting the in-cloud temperature and moisture fields in the analysis work to reduce the spin-up problem of forecast. In our experiments, the forecasts still undergo a period of adjustment, indicating the existence of inconsistencies among the model fields. More investigation on the nature of this adjustment is needed to further improve the cloud analysis procedure.

Acknowledgments. This work was mainly supported by NSF grants ATM-9909007, ATM-0129892 and a DOT-FAA grant via DOC-NOAA NA17RJ1227. Xue and Brewster were also supported by NSF grants ATM-0331756, ATM-0331594 and EEC-0313747, and Xue by "Outstanding Overseas Scholars" awards from Chinese Natural Science Foundation (No. 40028504) and from Chinese Academy of Sciences (No. 2004-2-7). Drs. Alan Shapiro and Bill Martin are thanked for very helpful discussions. ZXPLOT was used for the graphics. Supercomputers at OSCER, University of Oklahoma were used for most of the experiments.

References

Albers, S. C., J. A. McGinley, D. A. Birkenheuer, and J. R. Smart, 1996: The local analysis and prediction system (LAPS): Analysis of clouds, precipitation and temperature. *Wea. Forecasting*, **11,** 273-287.

Baldwin, M. E., S. Lakshmivarahan, and J. S. Kain, 2002: Development of an "events-oriented" approach to forecast verification. *15th Conf. Num. Wea. Pred.*, San Antonio, TX, Amer. Meteor. Soc.

Bratseth, A. M., 1986: Statistical interpolation by means of successive corrections. *Tellus*, **38A,** 439-447.

Brewster, K., 1996: Application of a Bratseth analysis scheme including Doppler radar data. *Preprints, 15th Conf. Wea. Anal. Forecasting*, Norfolk, VA, Amer. Meteor. Soc., 92-95.

Brewster, K., 2002: Recent advances in the diabatic initialization of a non-hydrostatic numerical model. *Preprints, 15th Conf on Numerical Weather Prediction and 21st Conf on Severe Local Storms*, San Antonio, TX, Amer. Meteor. Soc., J6.3.

Crum, T. D. and R. L. Alberty, 1993: The WSR-88D and the WSR-88D operational support facility. *Bull. Amer. Meteor. Soc.*, **74,** 1669-1687.

Droegemeier, K. K., 1990: Toward a science of storm-scale prediction. *Preprint, 16th conf. on Severe Local Storms*, Kananaskis Park, Alberta, Canada, Amer. Meteor. Soc., 256-262.

Droegemeier, K. K., 1997: The numerical prediction of thunderstorms: Challenges, potential benefits, and results from real time operational tests. *WMO Bulletin*, **46,** 324-336.

Gal-Chen, T., 1978: A method for the initialization of the anelastic equations: Implications for matching models with observations. *Mon. Wea. Rev.*, **106,** 587-606.

Gao, J., M. Xue, K. Brewster, F. Carr, and K. K. Droegemeier, 2002: New Development of a

3DVAR system for a nonhydrostatic NWP modeol. *Preprint, 15th Conf. Num. Wea. Pred. and 19th Conf. Wea. Anal. Forecasting*, San Antonio, TX, Amer. Meteor. Soc., 339-341.

Gao, J.-D., M. Xue, A. Shapiro, Q. Xu, and K. K. Droegemeier, 2001: Three-dimensional simple adjoint velocity retrievals from single Doppler radar. *J. Atmos. Ocean Tech.*, **18,** 26-38.

Gao, J.-D., M. Xue, K. Brewster, and K. K. Droegemeier, 2004: A three-dimensional variational data analysis method with recursive filter for Doppler radars. *J. Atmos. Ocean. Tech.*, **21,** 457-469.

Hu, M., M. Xue, and K. Brewster, 2005: 3DVAR and Cloud analysis with WSR-88D Level-II Data for the Prediction of Fort Worth Tornadic Thunderstorms. Part II: Impact of radial velocity analysis via 3DVAR. *Mon. Wea. Rev.***,** Conditionally accepted.

Kessler, E., 1969: *On the Distribution and Continuity of Water Substance in Atmospheric Circulations*. Vol. 32, *Meteor. Monogr.*, 84 pp.

Lilly, D. K., 1990: Numerical prediction of thunderstorms - Has its time come? *Quart. J. Roy. Meteor. Soc.*, **116,** 779-798.

Lin, Y.-L., R. D. Farley, and H. D. Orville, 1983: Bulk parameterization of the snow field in a cloud model. *J. Climate Appl. Meteor.*, **22,** 1065-1092.

Qiu, C. and Q. Xu, 1994: A spectral simple adjoint method for retrieving low-altitude winds from single-Doppler data. *J. Atmos. Oceanic Technology*, **11,** 927-936.

Qiu, C.-J. and Q. Xu, 1992: A simple adjoint method of wind analysis for single-Doppler data. *J. Atmos. Oceanic Tech.*, **9,** 588-598.

Rogers, R. R. and M. K. Yau, 1989: *A Short Course in Cloud Physics*. 3rd ed. Pergamon Press, 293 pp.

Schaefer, J. T., 1990: The critical success index as an indicator of warning skill. *Wea.*

Forecasting, **5,** 570-575.

Shapiro, A., S. Ellis, and J. Shaw, 1995: Single-Doppler radar retrievals with Phoenix II data: Clear air and microburst wind retrievals in the planetary boundary layer. *J. Atmos. Sci.*, **52,** 1265-1287.

Smith, P. L., Jr., C. G. Myers, and H. D. Orville, 1975: Radar reflectivity factor calculations in numerical cloud models using bulk parameterization of precipitation processes. *J. Appl. Meteor.*, **14,** 1156-1165.

Snyder, C. and F. Zhang, 2003: Assimilation of simulated Doppler radar observations with an ensemble Kalman filter. *Mon. Wea. Rev.*, **131,** 1663-1677.

Sun, J., D. W. Flicker, and D. K. Lilly, 1991: Recovery of three-dimensional wind and temperature fields from simulated single-Doppler radar data. *J. Atmos. Sci.*, **48,** 876-890.

Sun, J. and N. A. Crook, 1997: Dynamical and microphysical retrieval from Doppler radar observations using a cloud model and its adjoint. Part I: Model development and simulated data experiments. *J. Atmos. Sci.*, **54,** 1642-1661.

Sun, J. and N. A. Crook, 1998: Dynamical and Microphysical Retrieval from Doppler Radar Observations Using a Cloud Model and Its Adjoint. Part II: Retrieval Experiments of an Observed Florida Convective Storm. *J. Atmos. Sci.*, **55,** 835-852.

Tong, M. and M. Xue, 2005: Ensemble Kalman filter assimilation of Doppler radar data with a compressible nonhydrostatic model: OSS Experiments. *Mon. Wea. Rev.***,** In press.

Warner, J., 1970: On steady-state one-dimensional models of cumulus convection. *J. Atmos. Sci.*, **27,** 1035-1040.

Weygandt, S. S., A. Shapiro, and K. K. Droegemeier, 2002a: Retrieval of Model Initial Fields from Single-Doppler Observations of a Supercell Thunderstorm. Part I: Single-Doppler

Velocity Retrieval. *Mon. Wea. Rev.*, **130,** 433-453.

Weygandt, S. S., A. Shapiro, and K. K. Droegemeier, 2002b: Retrieval of Model Initial Fields from Single-Doppler Observations of a Supercell Thunderstorm. Part II: Thermodynamic Retrieval and Numerical Prediction. *Mon. Wea. Rev.*, **130,** 454-476.

Xu, Q., C. Qiu, and J. Yu, 1994: Adjoint-method retrievals of low-altitude wind fields from single-Doppler reflectivity measured during Phoenix II. *J. Atmos. Oceanic Technology*, **11,** 275-288.

Xue, M., K. K. Droegemeier, V. Wong, A. Shapiro, and K. Brewster, 1995: *ARPS Version 4.0 User's Guide*. [Available at http://www.caps.ou.edu/ARPS], 380 pp.

Xue, M., K. K. Droegemeier, and V. Wong, 2000: The Advanced Regional Prediction System (ARPS) - A multiscale nonhydrostatic atmospheric simulation and prediction tool. Part I: Model dynamics and verification. *Meteor. Atmos. Physics*, **75,** 161-193.

Xue, M., K. K. Droegemeier, V. Wong, A. Shapiro, K. Brewster, F. Carr, D. Weber, Y. Liu, and D. Wang, 2001: The Advanced Regional Prediction System (ARPS) - A multi-scale nonhydrostatic atmospheric simulation and prediction tool. Part II: Model physics and applications. *Meteor. Atmos. Phys.*, **76,** 143-166.

Xue, M., D.-H. Wang, J.-D. Gao, K. Brewster, and K. K. Droegemeier, 2003: The Advanced Regional Prediction System (ARPS), storm-scale numerical weather prediction and data assimilation. *Meteor. Atmos. Physics*, **82,** 139-170.

Zhang, F., C. , Snyder, and J. Sun, 2004: Impacts of initial estimate and observations on the convective-scale data assimilation with an ensemble Kalman filter. *Mon. Wea. Rev.*, **132,** 1238-1253.

Zhang, J., F. Carr, and K. Brewster, 1998: ADAS cloud analysis. *Preprints, 12th Conf. on Num.*

Wea. Pred., Phoenix, AZ., Amer. Met. Soc., 185-188.

Zhang, J., 1999: Moisture and Diabatic Initialization Based on Radar and Satellite Observation, Ph.D., School of Meteorology, University of Oklahoma, 194pp.

List of table

Table 1. The list of 3 km experiments and their main characteristics.

NAME	Temperature adjustment	Final analysis of hydrometeors	Initial determination of hydrometeors	Radar Data
CNTLZ	Moist adiabatic profile	Observation-based retrievals	SMO	Level II
X03	Latent heat	Maximum of Observation-based retrievals and background	KRY	Level III
CTLH	Latent heat	Observation-based retrievals	SMO	Level II
CKRY	Moist adiabatic profile	Observation-based retrievals	KRY	Level II
CMAX	Moist adiabatic profile	Maximum of Observation-based retrievals and background	SMO	Level II
NoVRZ	N.A.	N.A.	N.A.	No

List of Figures

interval is 5 dBZ. Counties around Fort Worth are labeled in (a).

Fig. 7. Similar to Fig. 6, except that they are predicted reflectivity from experiments X03 (left column) and CNTLZ (right column).

Fig. 8. Predicted surface wind and temperature fields from experiments X03 and CNTLZ at 0015 UTC and 0045 UTC 29 March, 2000. The domains shown are the same as in Fig. 6.

Fig. 9. Equitable threat scores of predicted reflectivity for the 5 (a), 15 (b), 30 (c), and 45 dBZ (d) threshold values from experiments CNTLZ and X03.

Fig. 10 Similar to Fig. 6, except that it is predicted reflectivity field from experiment NoVRZ at 0030 UTC 29 March, 2000.

Fig. 11. Reflectivity fields at 1.45° elevation of KFWS from assimilation results of experiments CNTLZ (b), X03 (c), CTLH (d), CKRY (e), and CMAX (f) and the corresponding radar observation (a). Major storm cells are marked by capital letters in (a). Tarrant County is highlighted and about 50×50 km^2 in size. The domain shown is about 200 km on each side, representing the portion of 3-km grid between 70 and 270 km in east-west direction and from 60 to 260 km in north-south direction. The reflectivity contours are at 15, 30, 45 and 55 dBZ and the shaded contour interval is 5 dBZ.

Fig. 12. Surface wind and temperature fields from assimilation results of experiments CNTLZ(b), X03(c), CTLH(d), CKRY(e), and CMAX(f) and background(a). The domains shown are the same as in Fig. 11.

Fig. 13. Cross section (along line in Fig. 11a) of vertical velocity fields from assimilation results of experiments X03(a), CNTLZ(b), CKRY(c), CTLH(d), and CMAX(e).

Fig. 14. Similar to Fig. 6, except that they are predicted reflectivity from experiments CMAX, CKRY and CTLH at 0015 UTC and 0045 UTC 29 March, 2000.

Fig. 15. Similar to Fig. 8, except that they are from experiments CMAX, CKRY and CTLH at 0015 UTC and 0045 UTC 29 March, 2000.

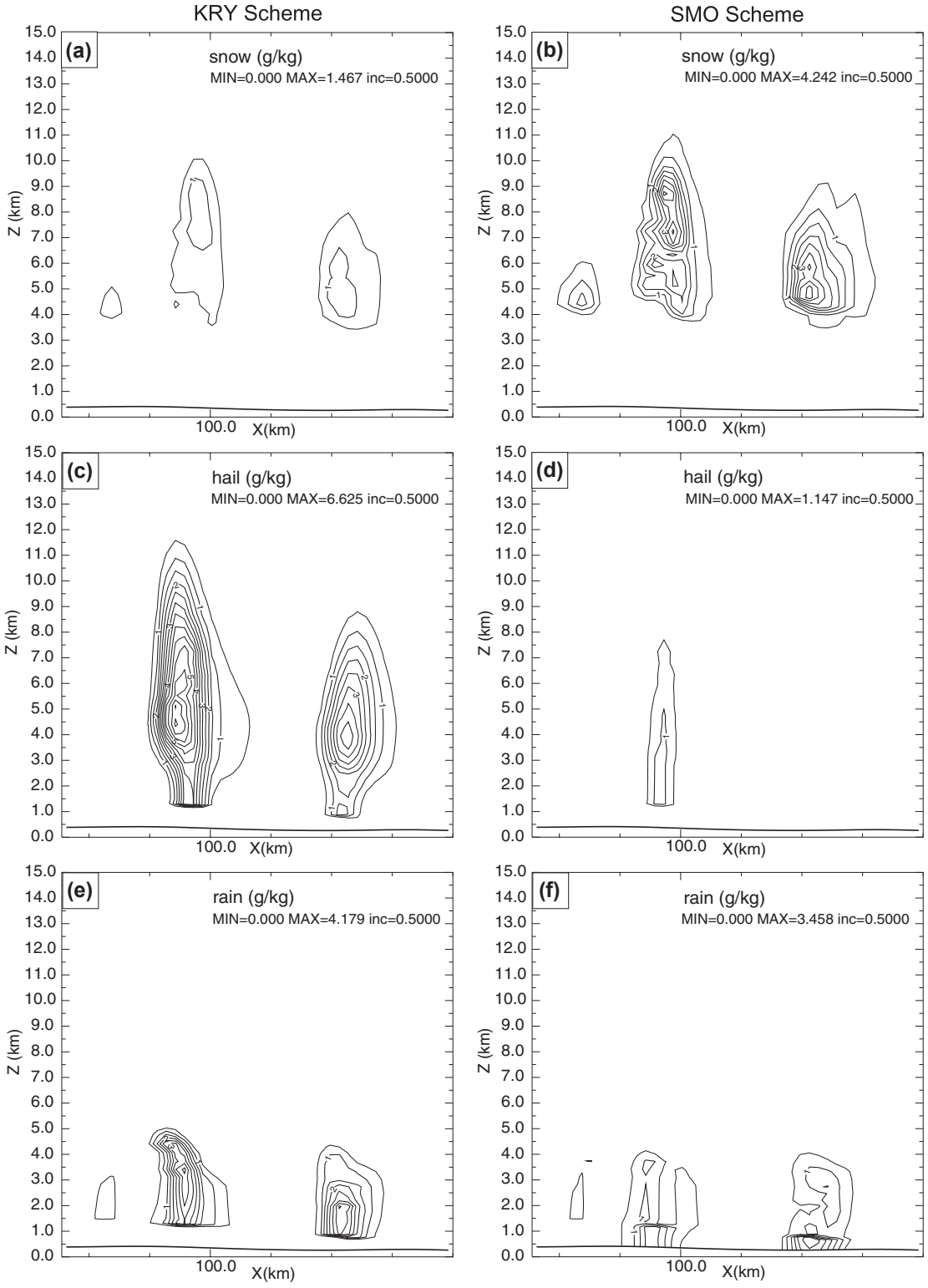

Fig. 1. Cross sections of snow, hail, and rain fields determined from reflectivity observations by the KRY (left) and SMO (right) schemes using the background analysis, for 2250 UTC, 28 March, 2000.

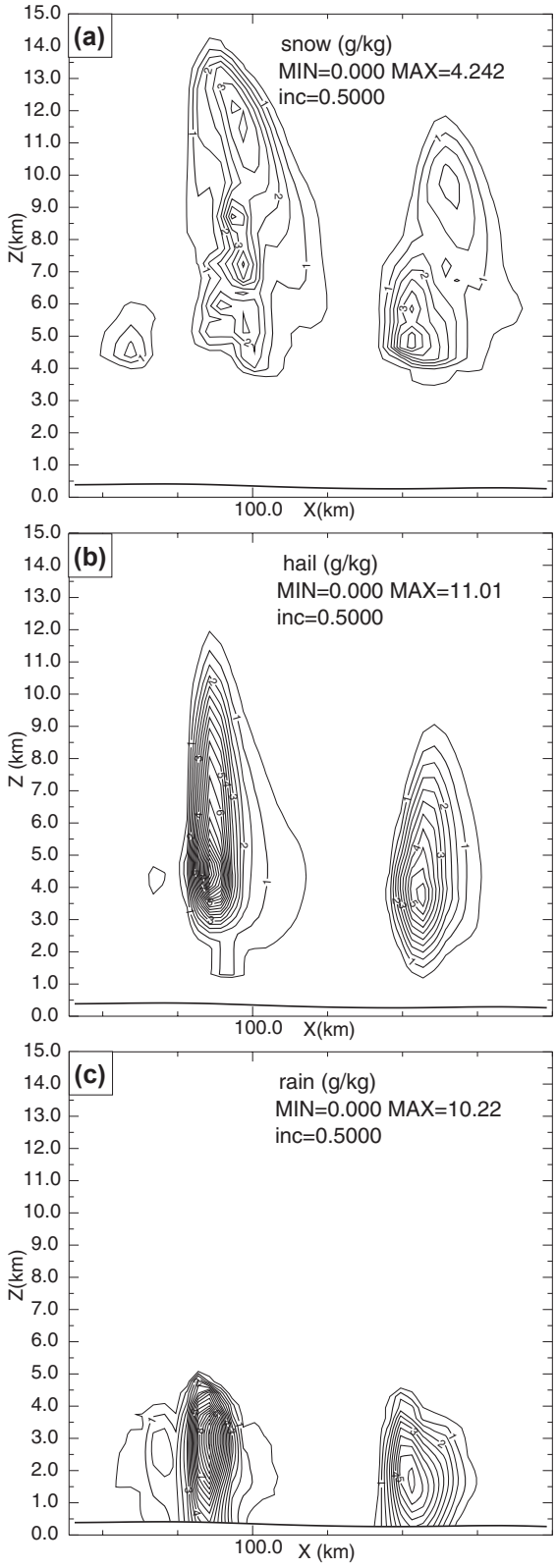

Fig. 2. Cross section of final analysis of snow, hail, and rain fields by the cloud analysis used by Xue03, for 2250 UTC, 28 March, 2000.

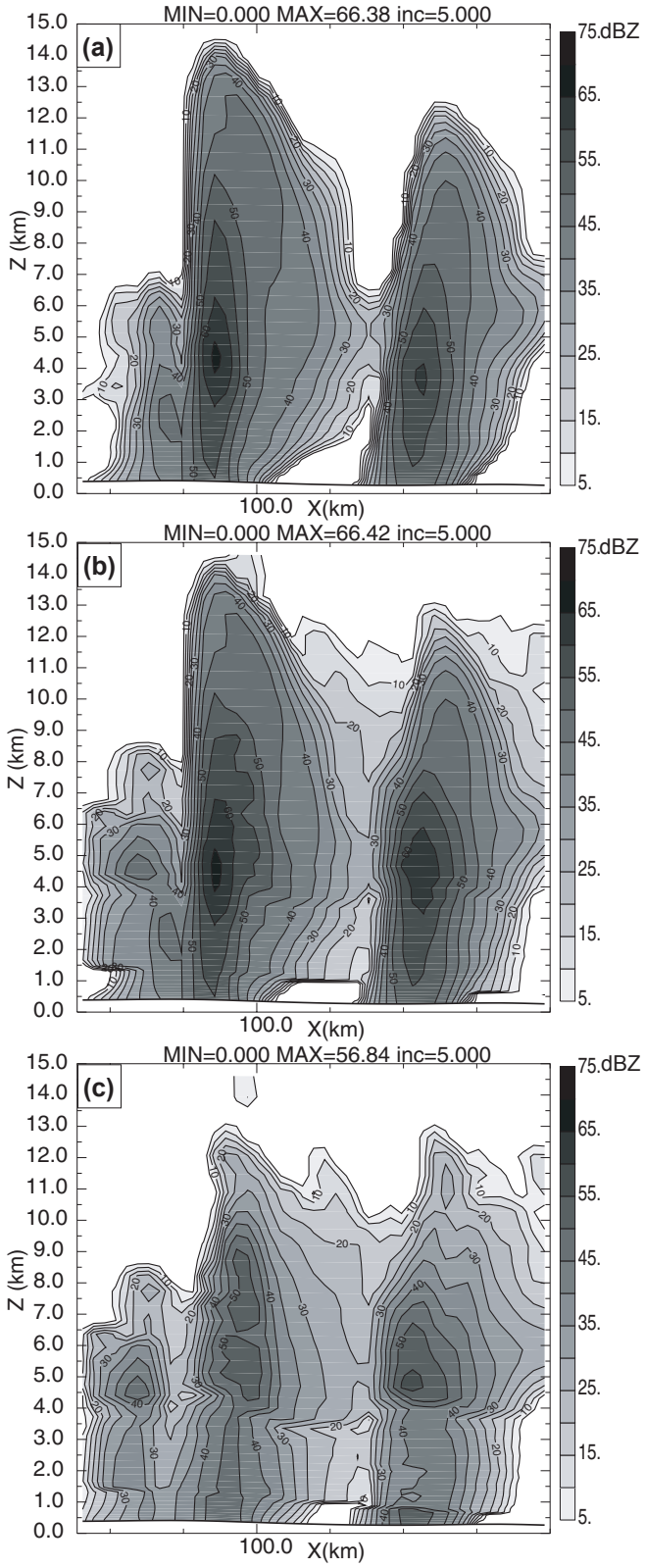

Fig. 3. Cross section of reflectivity fields calculated from precipitation mixing ratios of, a) background; b) the cloud analysis of Xue03; c) the updated cloud analysis, for 2250 UTC, 28 March, 2000.

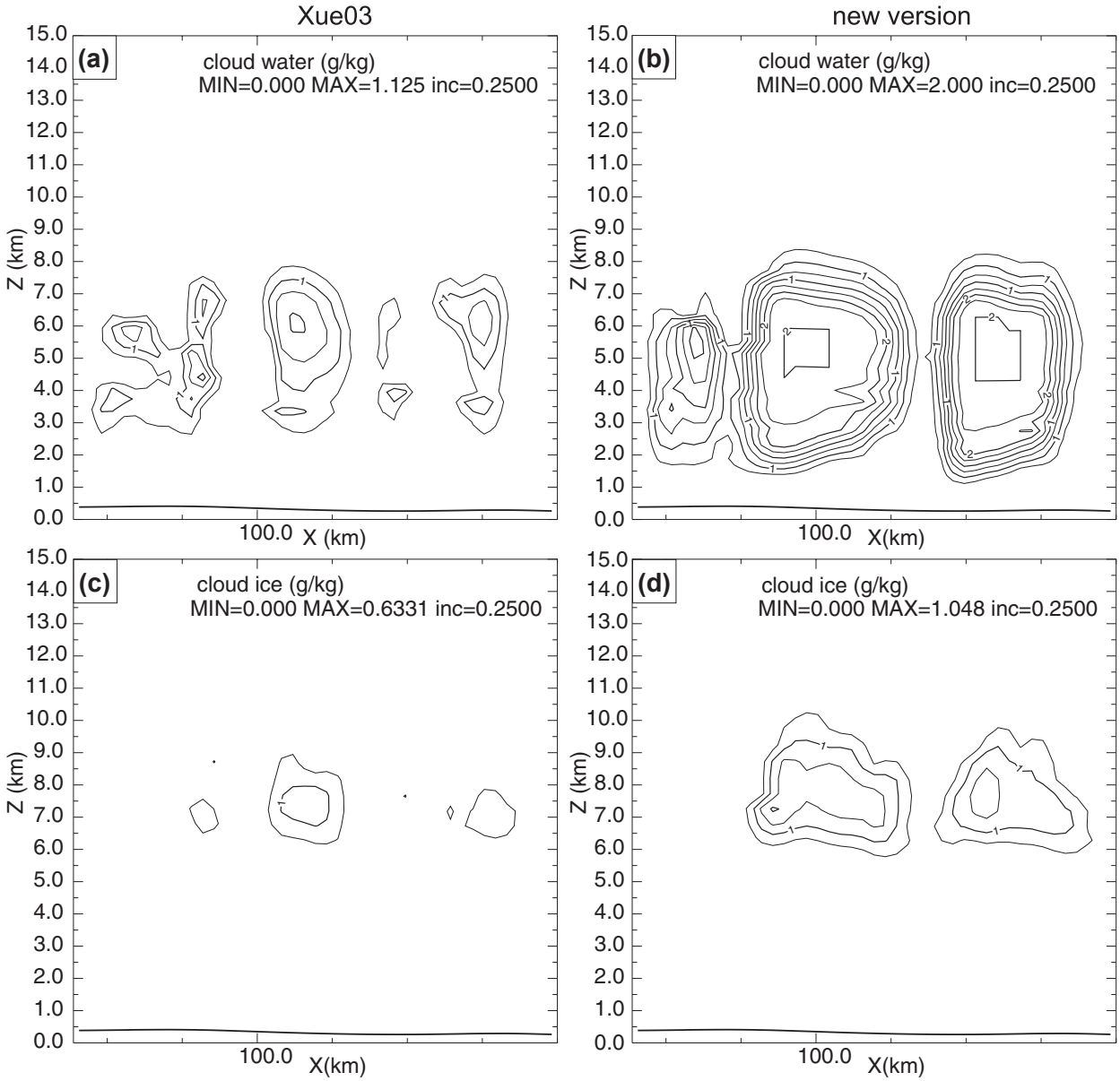

Fig. 4. Cross section of cloud water and cloud ice fields from the cloud analysis with the entrainment curve used in Xue03 (left) and the new curve (right) with reduced entrainment, for 2250 UTC, 28 March, 2000.

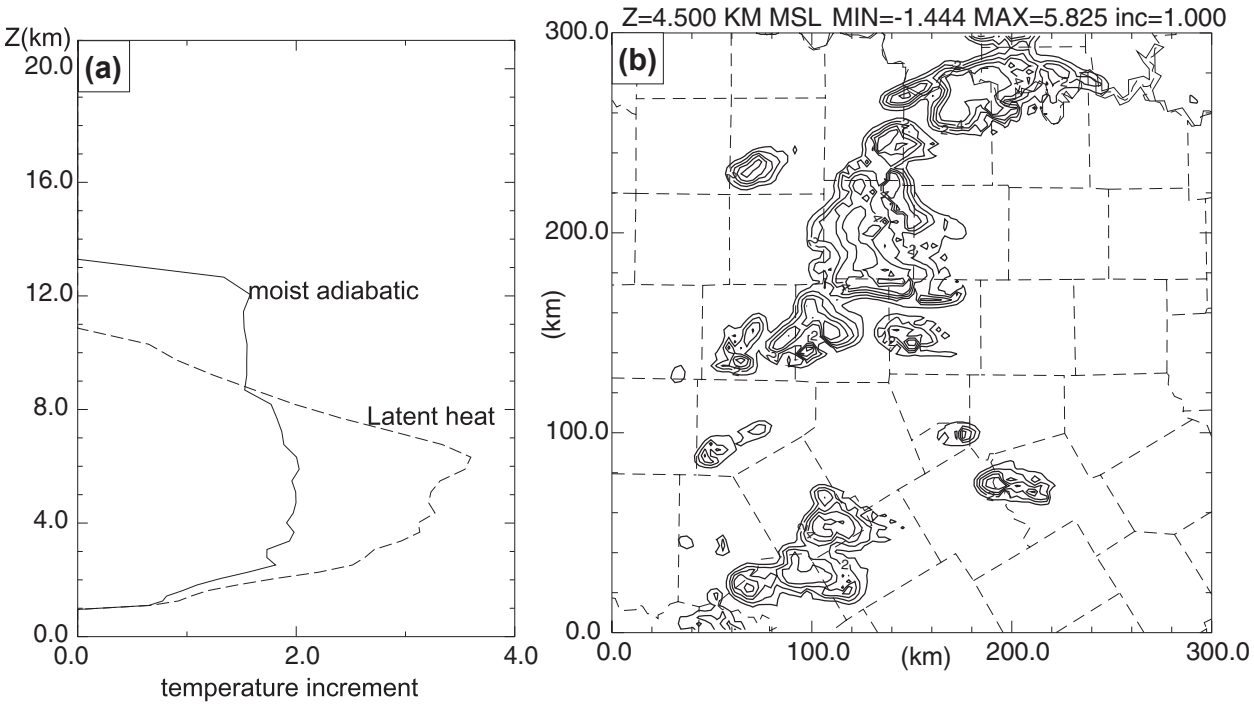

Fig. 5. The profile of horizontally averaged temperature increments from adjustments using the moist adiabatic profile (of the updated version) and latent heat (used in Xue03) methods (a), and the difference in the temperature increment between these two methods at 4.5 km MSL (b), for 2250 UTC, 28 March, 2000.

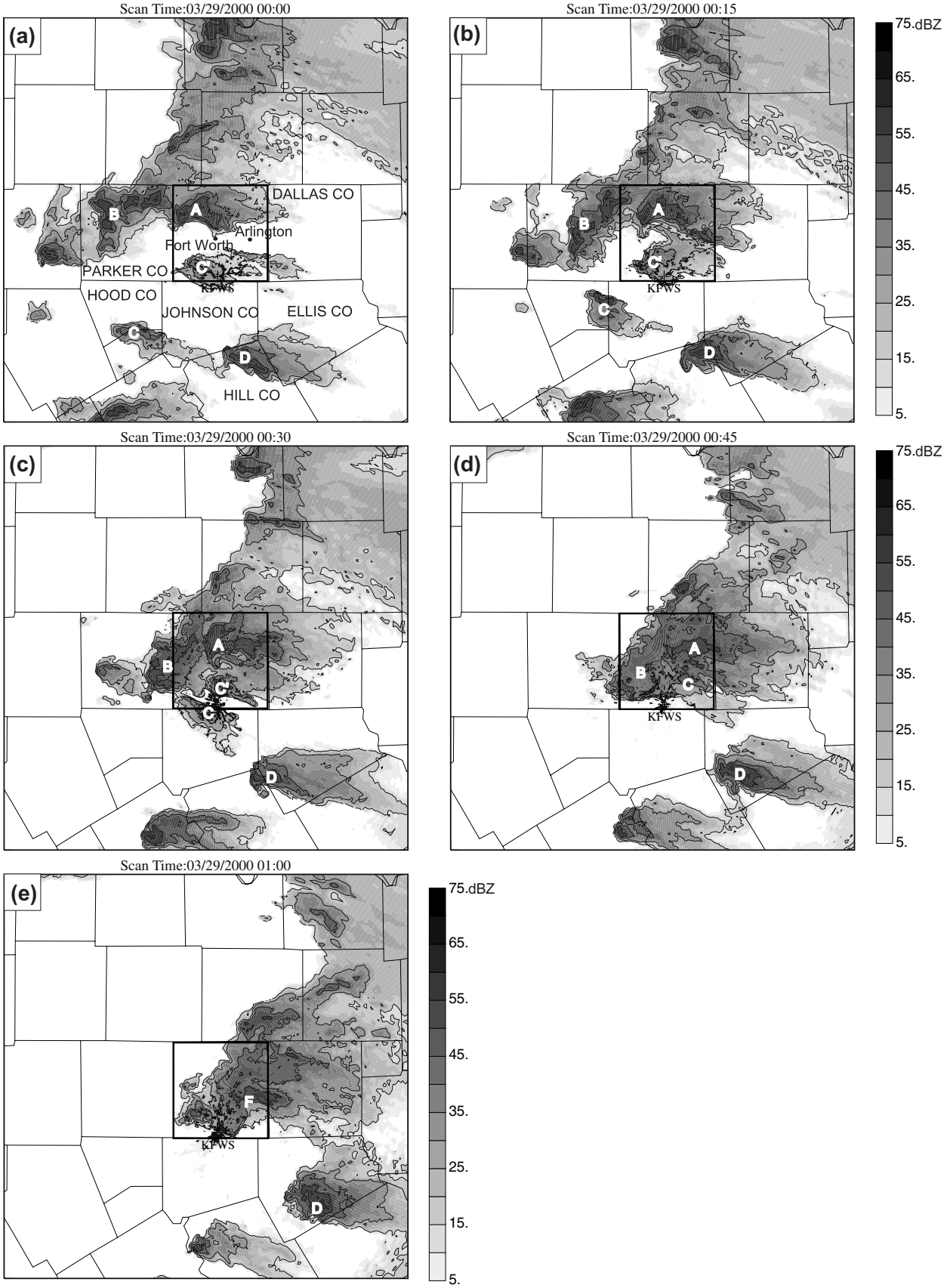
Scan Time:03/29/2000 00:00
(a)
DALLAS CO
Arlington
Fort Worth
PARKER CO
HOOD CO
JOHNSON CO
ELLIS CO
HILL CO
KFWS
A
B
C
D
Scan Time:03/29/2000 00:15
(b)
Scan Time:03/29/2000 00:30
(c)
Scan Time:03/29/2000 00:45
(d)
Scan Time:03/29/2000 01:00
(e)
F
75.dBZ
65.
55.
45.
35.
25.
15.
5.

Fig. 6. Observed reflectivity fields at 1.45° elevation of the Fort Worth radar (marked as KFWS) based on Level-II data, at 15 minute intervals from 0000 UTC to 0100 UTC 29 March, 2000. Major storm cells are marked by capital letters. Fort Worth and Arlington are marked as dots in (a). Tarrant County is highlighted and about 50×50 km^2 in size. The domain shown is about 200 km on each side, representing the portion of 3-km grid between 100 and 300 km in east-west direction and from 60 to 260 km in north-south direction. The reflectivity contours are at 15, 30, 45 and 55 dBZ and the shaded contour interval is 5 dBZ. Counties around Fort Worth are labeled in (a).

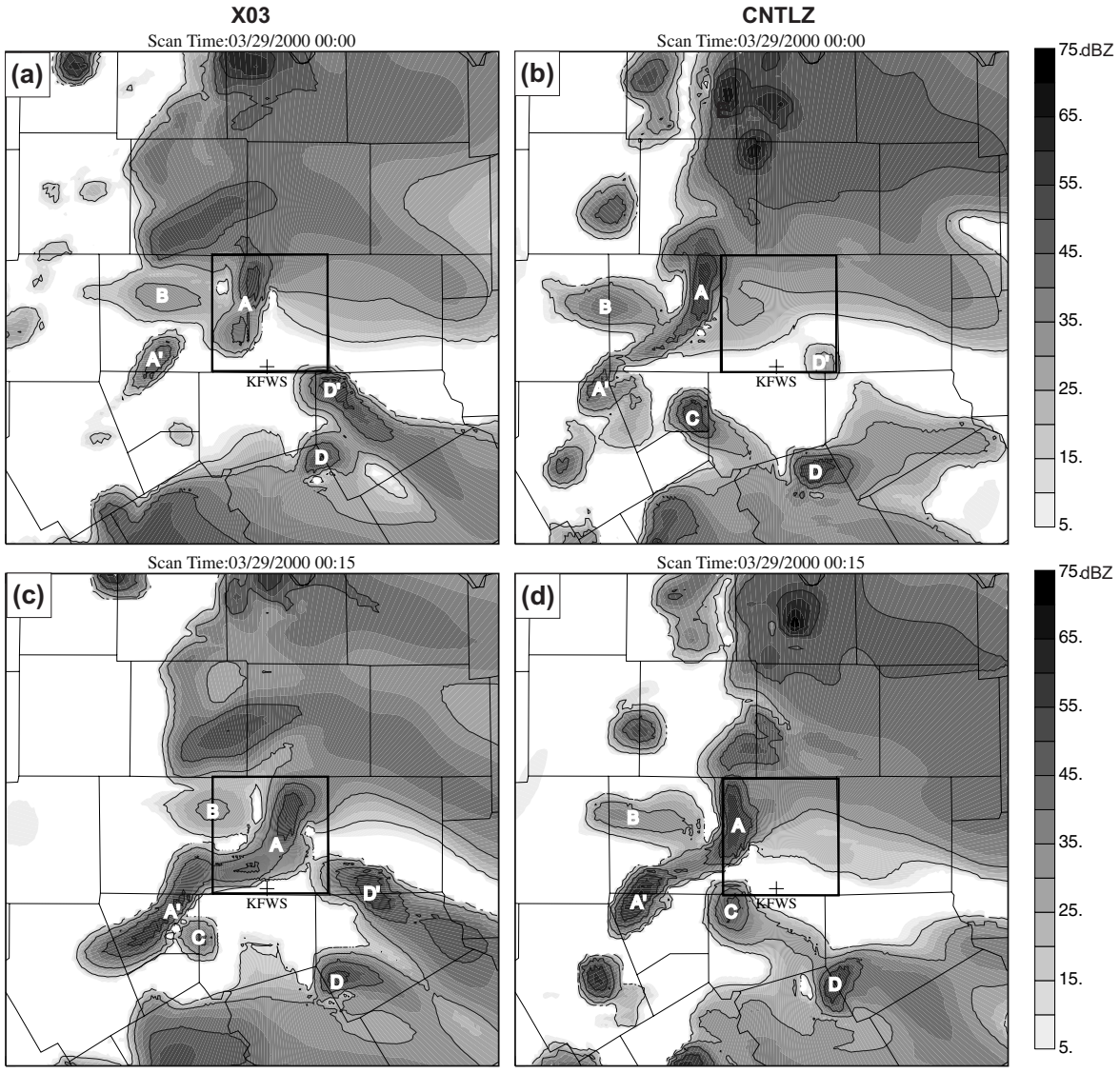

Fig. 7. Similar to Fig. 6, except that they are predicted reflectivity from experiments X03 (left column) and CNTLZ (right column).

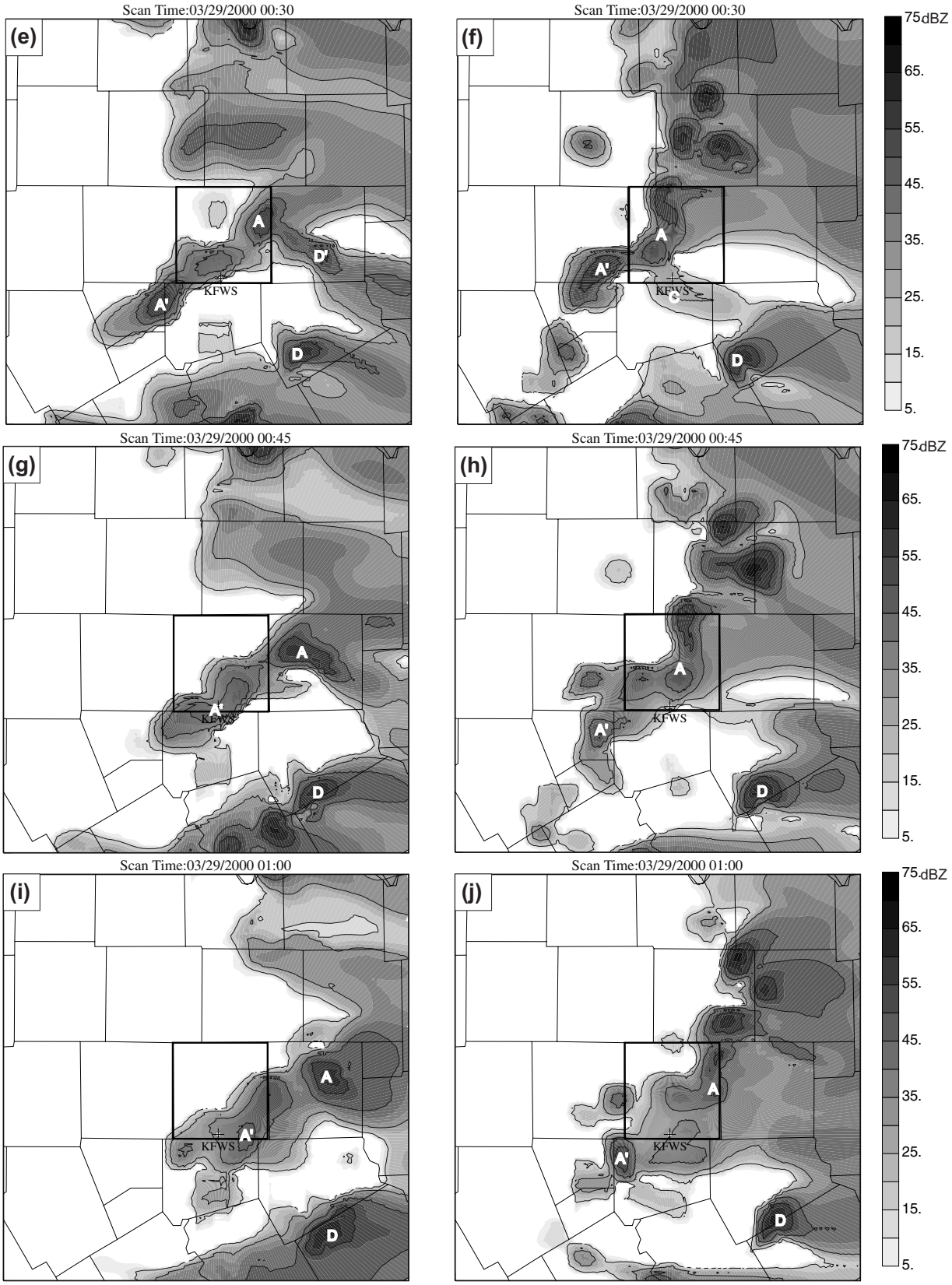

Fig. 7. Continued.

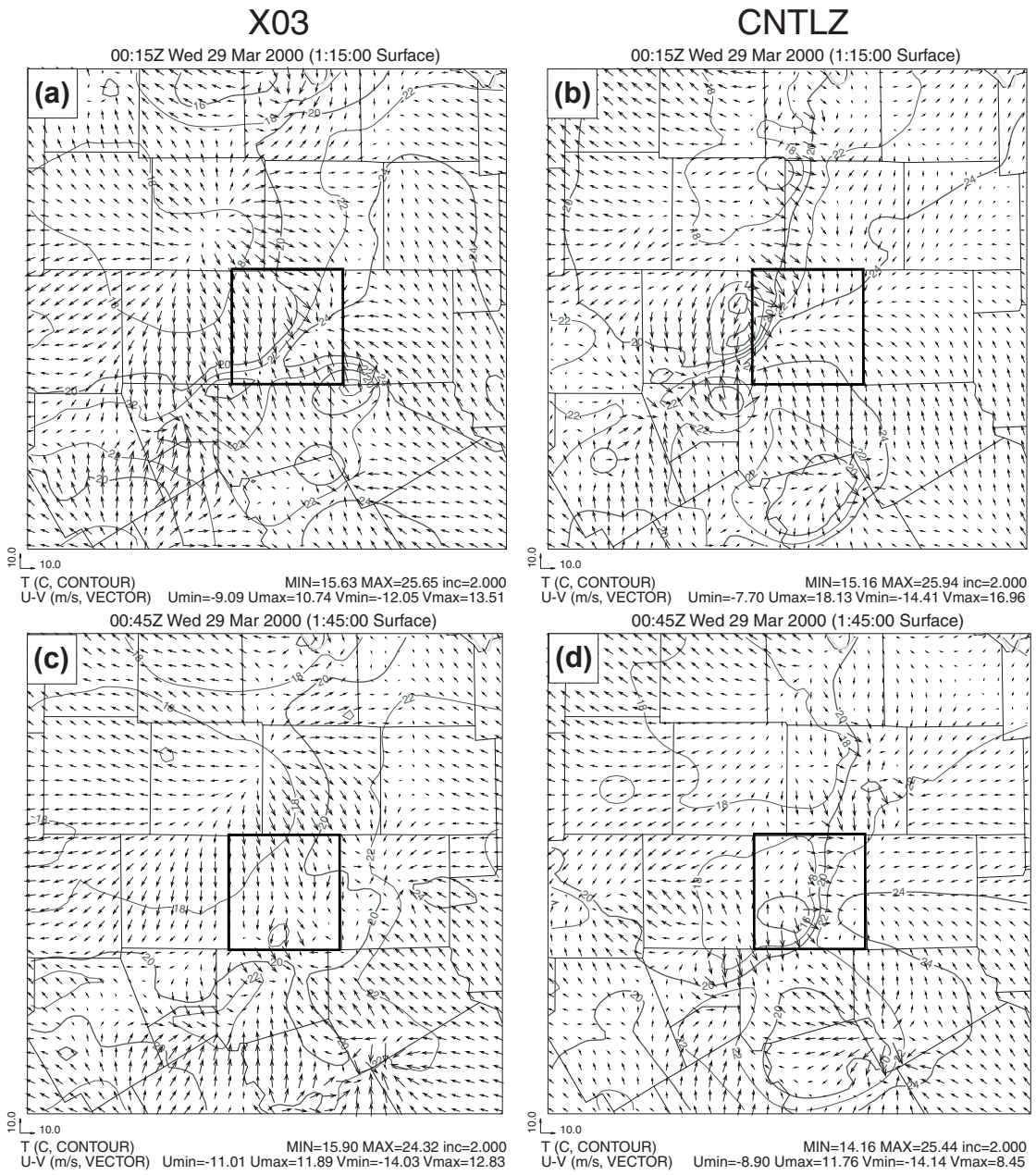

Fig. 8. Predicted surface wind and temperature fields from experiments X03 and CNTLZ at 0015 UTC and 0045 UTC 29 March, 2000. The domains shown are the same as in Fig. 6.

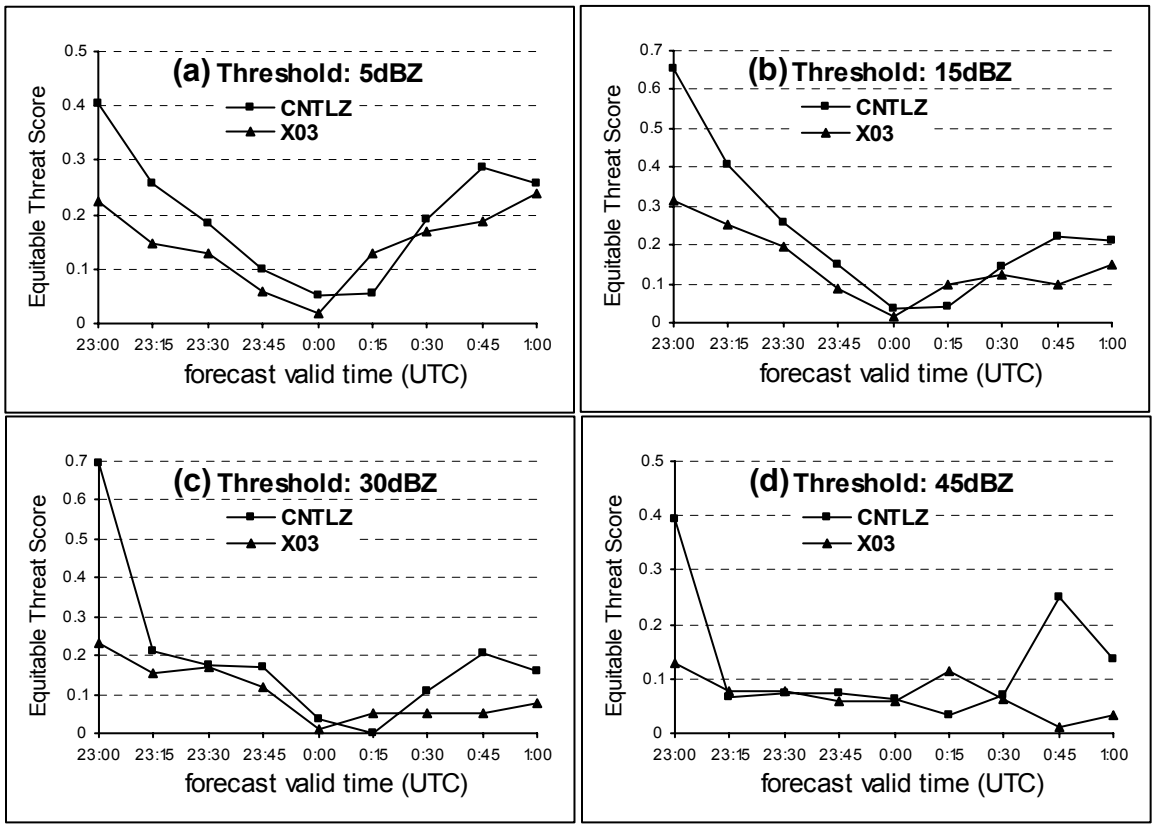

Fig. 9. Equitable threat scores of predicted reflectivity for the 5 (a), 15 (b), 30 (c), and 45 dBZ (d) threshold values from experiments CNTLZ and X03.

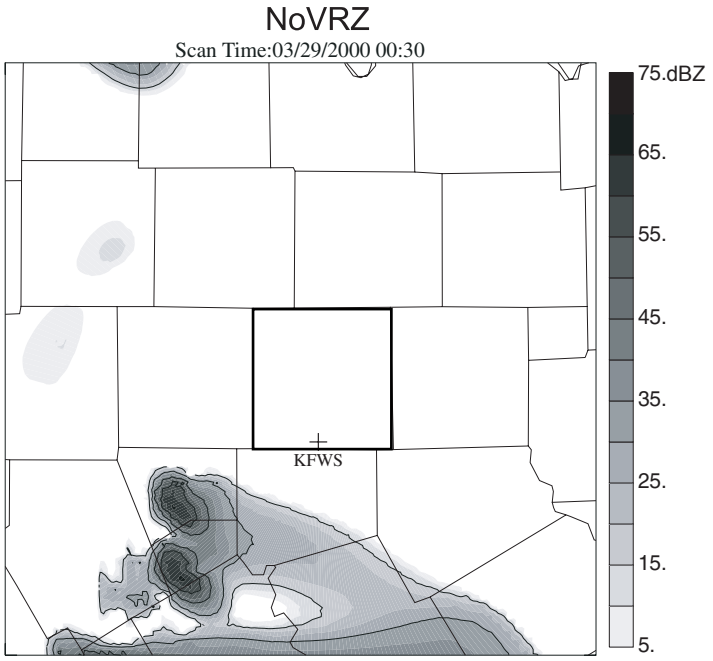

Fig. 10 Similar to Fig. 6, except that it is predicted reflectivity field from experiment NoVRZ at 0030 UTC 29 March, 2000.

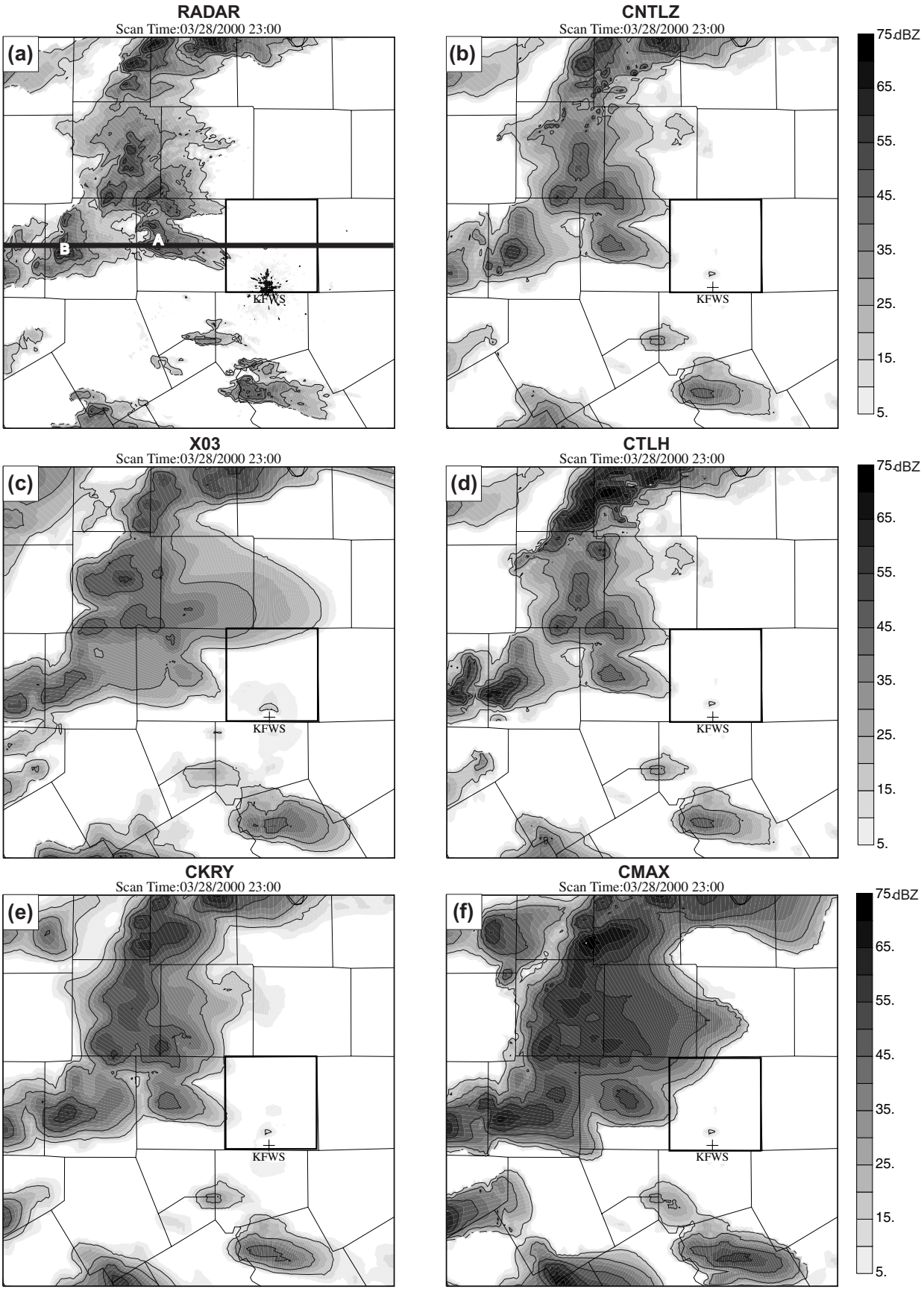
RADAR
Scan Time:03/28/2000 23:00
(a)
B
A
KFWS
CNTLZ
Scan Time:03/28/2000 23:00
(b)
KFWS
75 dBZ
65.
55.
45.
35.
25.
15.
5.
X03
Scan Time:03/28/2000 23:00
(c)
KFWS
CTLH
Scan Time:03/28/2000 23:00
(d)
KFWS
CKRY
Scan Time:03/28/2000 23:00
(e)
KFWS
CMAX
Scan Time:03/28/2000 23:00
(f)
KFWS

Fig. 11. Reflectivity fields at 1.45° elevation of KFWS from assimilation results of experiments CNTLZ (b), X03 (c), CTLH (d), CKRY (e), and CMAX (f) and the corresponding radar observation (a). Major storm cells are marked by capital letters in (a). Tarrant County is highlighted and about 50×50 km^2 in size. The domain shown is about 200 km on each side, representing the portion of 3-km grid between 70 and 270 km in east-west direction and from 60 to 260 km in north-south direction. The reflectivity contours are at 15, 30, 45 and 55 dBZ and the shaded contour interval is 5 dBZ.

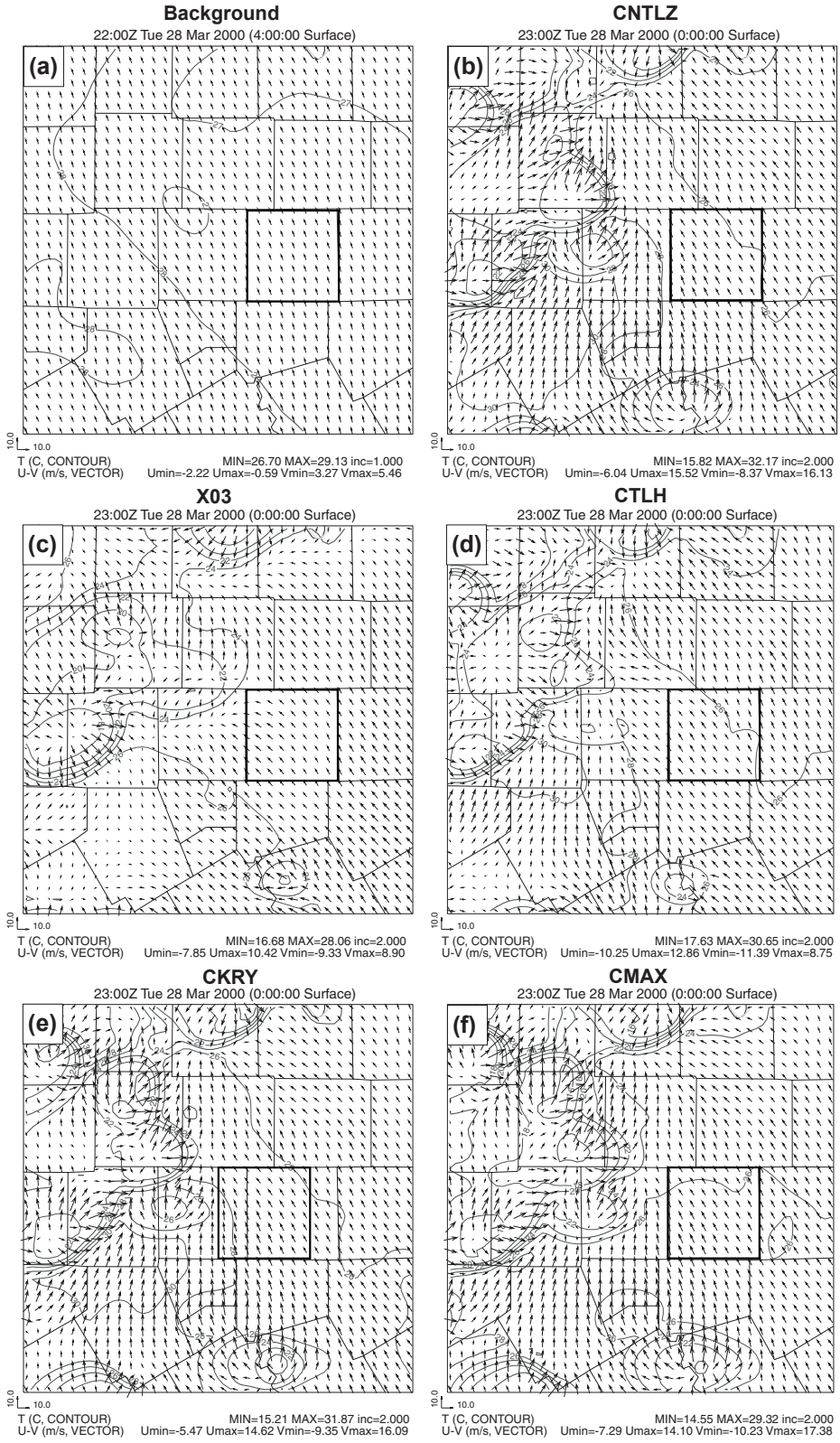

Fig. 12. Surface wind and temperature fields from assimilation results of experiments CNTLZ(b), X03(c), CTLH(d), CKRY(e), and CMAX(f) and background(a). The domains shown are the same as in Fig. 11.

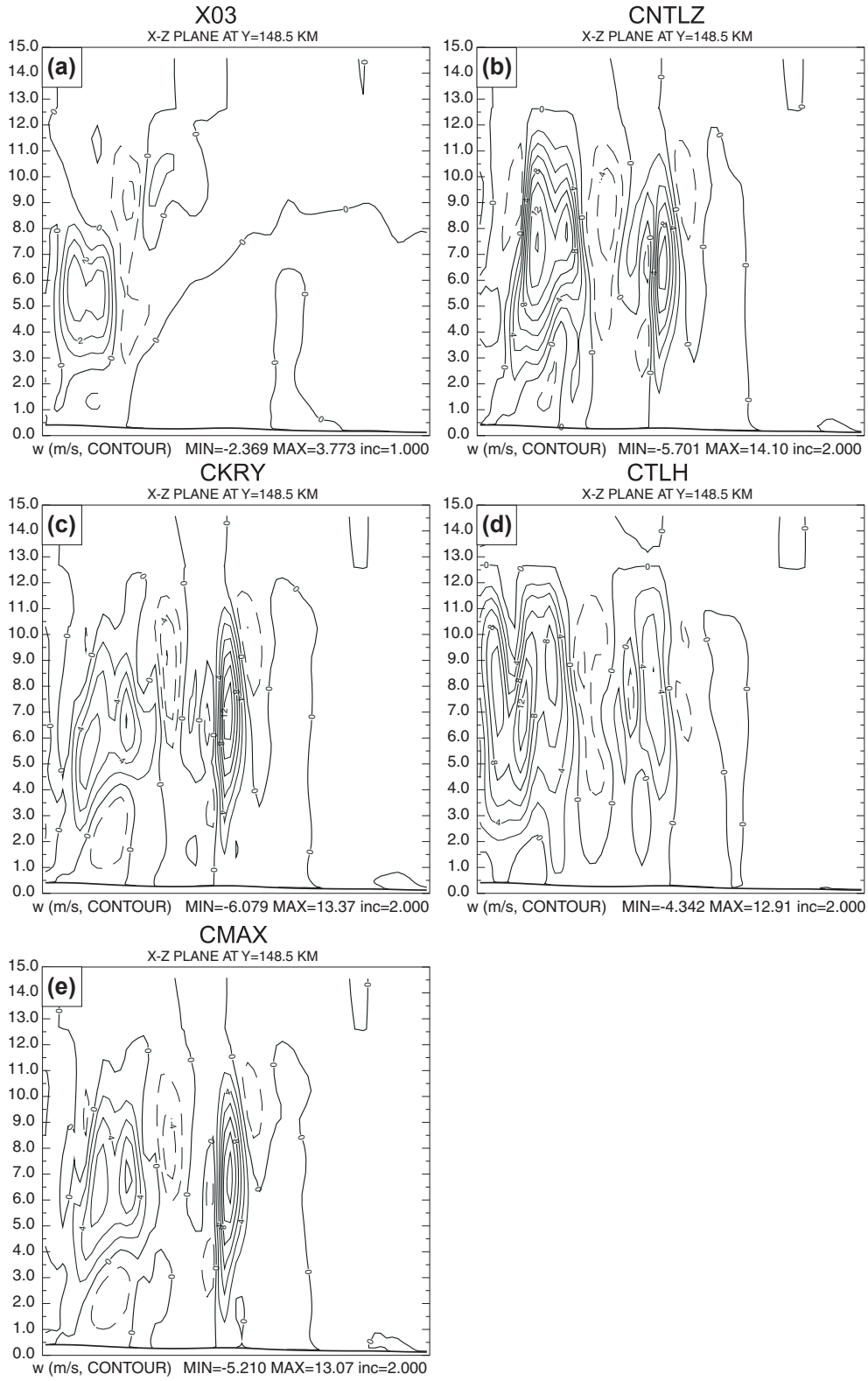

Fig. 13. Cross section (along line in Fig. 11a) of vertical velocity fields from assimilation results of experiments X03(a), CNTLZ(b), CKRY(c), CTLH(d), and CMAX(e).

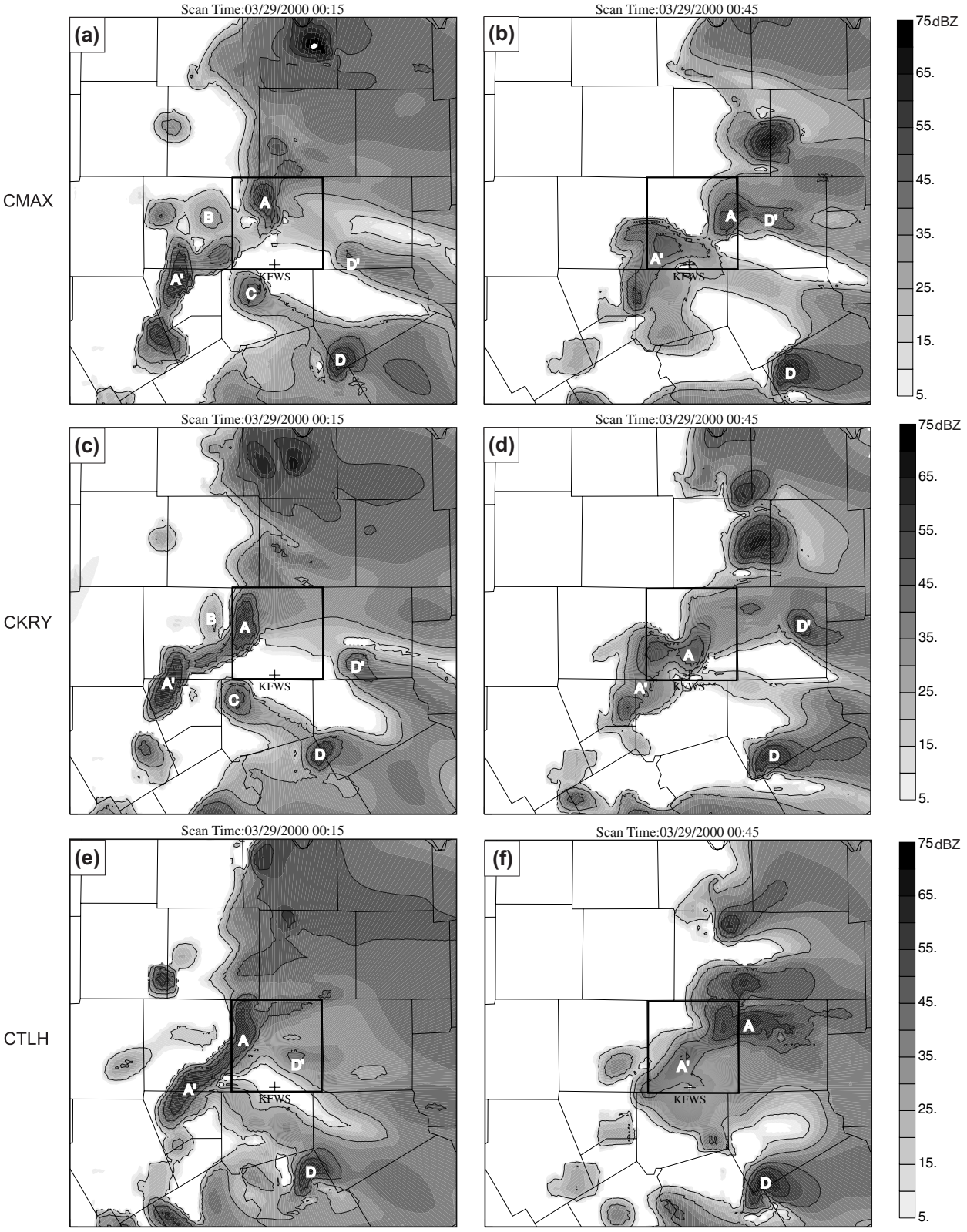

Fig. 14. Similar to Fig. 6, except that they are predicted reflectivity from experiments CMAX, CKRY and CTLH at 0015 UTC and 0045 UTC 29 March, 2000.

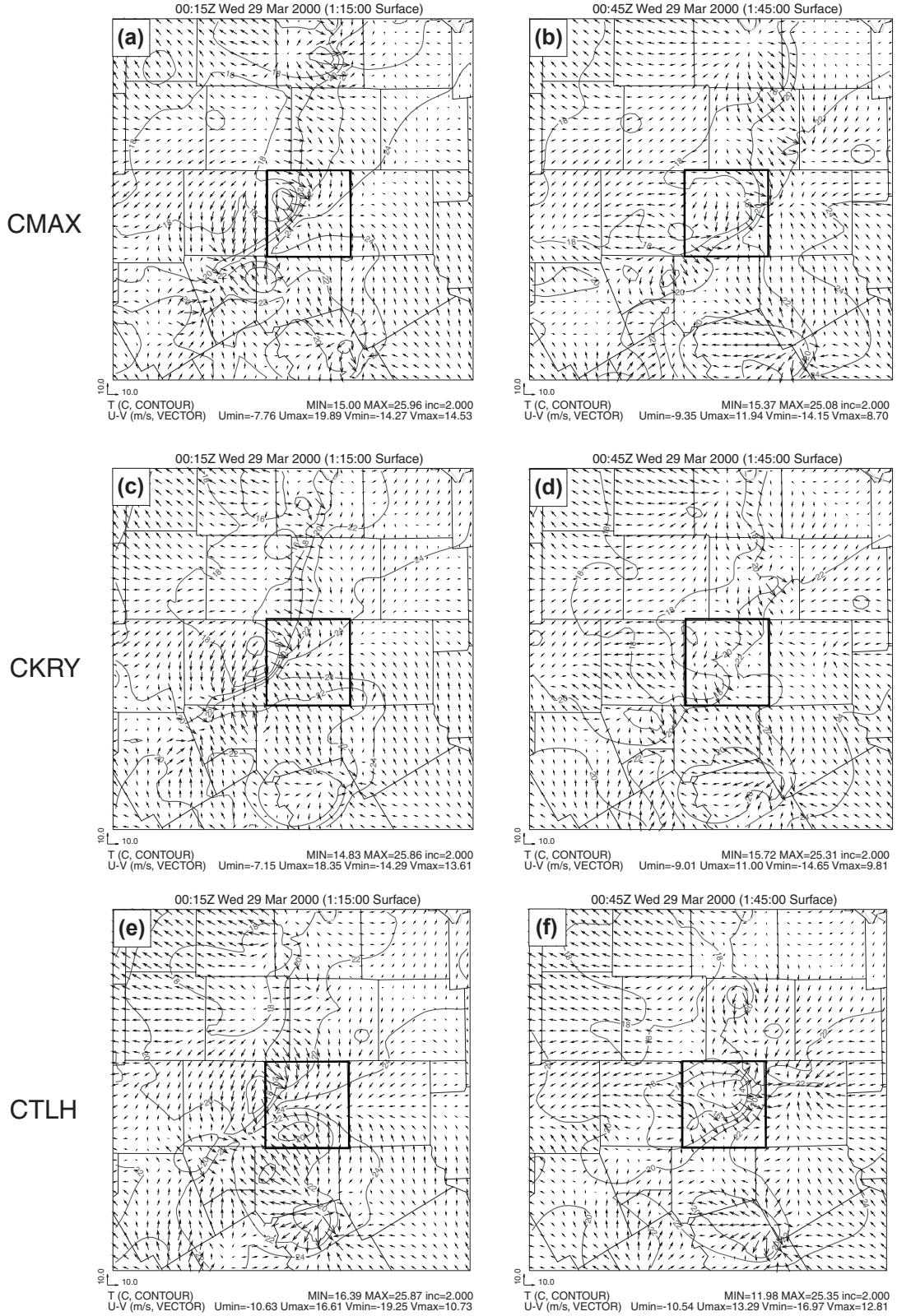

Fig. 15. Similar to Fig. 8, except that they are from experiments CMAX, CKRY and CTLH at 0015 UTC and 0045 UTC 29 March, 2000.